Science
AAAS

Supplementary Materials for

Cyclic ADP ribose isomers: Production, chemical structures, and immune signaling

Mohammad K. Manik *et al*.

Corresponding authors: Thomas Ve, t.ve@griffith.edu.au; Bostjan Kobe, b.kobe@uq.edu.au

Science **377**, eadc8969 (2022)
DOI: 10.1126/science.adc8969

The PDF file includes:

Other Supplementary Material for this manuscript includes the following:

Materials and Methods

Cloning

AbTir: ligation-independent cloning (LIC) (*55*) was used to generate AbTir constructs. Full-length AbTir cDNA (GenBank: EXB04249.1) was obtained as a gBlock (Integrated DNA Technologies). $AbTir^{full\text{-}length}$ (amino acid 1-269), $AbTir^{CC}$ (amino acid 27-118) and $AbTir^{TIR}$ (amino acid 134-267) were amplified using AccuPower® Pfu PCR PreMix (Bioneer Pacific). Crystallization Construct Designer (https://ccd.rhpc.nki.nl/) was used to design all primers (*56*). The forward and reverse primers had the following overhangs, respectively: Fw: TACTTCCAATCCAATGCG; Rv: TTATCCACTTCCAATGTTA . The amplified products and SSpI (NEB Cat # R0132S)-digested pMCSG7 plasmids (*57*) were treated with T4 DNA polymerase (NEB). Subsequently, 2 µl of T4 DNA polymerase-treated PCR product, and pMCSG7 were incubated at room temperature for 30 minutes. The mixtures were then transformed into *E. coli* (DH5α) competent cells using a lysogeny broth (LB) agar plate containing 100 µg/mL ampicillin. The LB plate was then incubated for 16 hours at 37°C. *E. coli* colonies having the plasmids were confirmed by colony PCR using AccuPower® Taq PCR Premix (Bioneer Pacific). Four successfully transformed colonies were then grown in 10 mL LB containing 100 µg/mL ampicillin (Sigma-Aldrich) in a 50 mL Falcon tube for 16 h at 37°C. Plasmids were extracted from the cultures using QIAprep® Spin Miniprep Kit from Qiagen. Then, all constructs were sequenced using the AGRF (Australian Genome Research Centre) Sanger sequencing service.

ThsA proteins: Full-length BcThsA (WP_002078322.1), $BcThsA^{SIR2}$ (residues 1-284), $BcThsA^{SLOG}$ (284-476), AbThsA (WP_032061149), EfThsA (WP_230207162), SeThsA (WP_012679271), and $SeThsA^{SIR2}$ (residues 1-283) were synthesized (gBlock, Integrated DNA Technologies) and cloned into the pMCSG7 vector using LIC (*57*).

AbTir, AaTir, BtTir, BXY39700, BtTir, Bovatus_RS22005, AMN69_RS28245, DORFOR_RS09155, PROVRUST_05034, AMN69_RS06490, CLOBOL_01188 for HPLC assays: DNA fragments encoding TIR domains codon-optimized for *E. coli* expression were synthesized and cloned into the pET30a vector, in between NheI and HindIII restriction sites, with an N-terminal tandem Strep-tag and a C-terminal 6x-histidine tag.

Site-directed mutagenesis

All $AbTir^{TIR}$ mutants were prepared by using a pair of complementary primers with the desired mutation, and $AbTir^{TIR}$ (amino acids 134-267) in the pMCSG7 vector was used as the template. The plasmid DNA with the desired mutation was amplified using AccuPower® Pfu PCR PreMix from Bioneer Pacific. The amplified PCR products were then purified using the QIAquick PCR Purification Kit (Qiagen). The purified PCR products were then treated with DpnI (NEB Cat # R0176S) to destroy the template DNA. After DpnI digestion, *E. coli* (DH5α) competent cells were transformed with the plasmid DNA. All the colonies were screened, and the purified plasmids were sequenced using the same method as described in the cloning section.

EfThsA mutants were produced using Q5® Site-Directed Mutagenesis (New England BioLabs), while SeThsA mutants were synthesized (gBlock, Integrated DNA Technologies) and cloned into the pMCSG7 vector using LIC (*57*). Pure plasmids were prepared using the QIAprep Spin Miniprep Kit (Qiagen) and the sequences confirmed by the Australian Genome Research Facility.

Protein expression

AbTir, AbTir^{TIR} and AbTir^{CC}: For protein expression, BL21-Gold (DE3) Competent Cells (Agilent Technologies, Inc.) were transformed using the desired plasmid and grown on a LB-ampicillin (100 µg/mL) plate. The next day, 10 mL starter culture was grown for 16 hours at 37ºC in LB media containing 100 µg/mL ampicillin. The following day, 1 mL of the 16-hour culture was added to 1 L autoclaved LB-ampicillin (100 µg/mL) media in 2.5 L ultra-yield flasks (Thomson's Ultra Yield Flasks™, Genesearch). The flasks were incubated at 37°C in a shaking incubator (New Brunswick™ Innova® 44) at 225 rpm, until OD_{600} reached 0.6-0.8. After that, IPTG (isopropyl β-D-1-thiogalactopyranoside) (Merck Millipore) was added to a final concentration of 1 mM and the cultures incubated for 12-16 hours at 15°C.

AaTir^{TIR}, BtTir^{TIR} and ThsA proteins: AaTir^{TIR} (residues 2-144, WP_091411838) and BtTir^{TIR} (residues 156-287, WP_048697596) in the pET30a vector (N-terminal tandem Strep-tag and C-terminal His_6-tag), and BcThsA, BcThsA^{SIR2}, BcThsA^{SLOG} AbThsA, EfThsA, SeThsA and SeThsA^{SIR2} in the pMCSG7 vector (N-terminal His_6-tag, TEV (tobacco etch virus) protease cleavage site) were produced in *E. coli* BL21 (DE3) cells, using the autoinduction method (*58*) and purified to homogeneity, using a combination of immobilized metal-ion affinity chromatography (IMAC) and size-exclusion chromatography (SEC). The cells were grown at 37°C, until an OD^{600} of 0.6- 0.8 was reached. The temperature was then reduced to 20°C, and the cells were grown overnight for approximately 16 h. The cells were harvested by centrifugation at 5000 x *g* at 4°C for 15 min and stored at −80°C until used for purification.

Protein purification

AbTir, AbTir^{TIR} and AbTir^{CC}: Cells were harvested by centrifuging at 4000 rpm (Beckman Coulter J-26 XPI, JLA 9.1 rotor) for 20 min at 4ºC. After centrifugation, the supernatant was discarded, and the cell pellet was resuspended in ice-cold lysis/wash buffer (3 mL/L) (2X PBS, 300 mM NaCl, 30 mM imidazole, 1 mM PMSF (phenylmethanesulfonylfluoride). Bacterial cell lysis was performed by using sonication (Branson, 10 seconds pulse, 10 seconds off at 40% amplitude). Lysed samples were then centrifuged (Beckman Coulter J-26 XPI, JA 20 rotor) for 40 minutes at 4ºC to remove the cell debris, and the supernatant was loaded onto a 5 mL HisTrap column (GE Healthcare) at 4 mL/min. After that, the column was washed using 20 column volumes (CVs) of ice-cold lysis/wash buffer (3 mL/L) (2X PBS, 300 mM NaCl, 30 mM imidazole, 1 mM PMSF). The protein was eluted using 10 CVs of elution buffer (100 mM Hepes pH 8.0, 500 mM NaCl, 500 mM imidazole). The eluted samples were then analyzed by 15% SDS-PAGE, and fractions containing pure proteins were pooled and dialyzed for 30 minutes in dialysis buffer (2X PBS, 1 mM DTT) at 4°C, to remove imidazole. After 30 minutes, TEV protease was added and incubated overnight at 4°C to remove the His-tag. The next day, the dialyzed samples were passed through a 5 mL HisTrap column (GE Healthcare) to remove the TEV protease. Then, the sample was further purified using size-exclusion chromatography (SEC) using the S75 HiLoad 26/600 column (GE Healthcare), pre-equilibrated with the gel-filtration buffer (10 mM HEPES pH 8.0, 150 mM NaCl). SEC was performed using ÄKTAprime or ÄKTA pure (GE Healthcare) systems.

AaTir^{TIR}, BtTir^{TIR}, BcThsA, AbThsA, EfThsA and SeThsA: The cells were harvested by centrifugation at 5000 x *g* at 4°C for 15 min, the cell pellets were resuspended in 2-3 mL of lysis buffer (50 mM HEPES pH 8.0, 500 mM NaCl) per g of cells. The resuspended cells were lysed using a digital sonicator and clarified by centrifugation (15,000 x *g* for 30 minutes). The clarified lysate was supplemented with imidazole (final concentration of 30 mM) and then applied to a nickel HisTrap column (Cytiva) pre-equilibrated with 10 CVs of the wash buffer (50 mM HEPES pH 8.0, 500 mM NaCl, 30 mM imidazole) at a rate of 4 mL/min. The column was washed with 10 CVs of the wash buffer followed by elution of bound proteins using elution buffer (50 mM HEPES pH 8, 500 mM NaCl, 250 mM imidazole). The elution fractions were analysed by SDS-PAGE and

the fractions containing the protein of interest were pooled and further purified on either a S75 HiLoad 26/600 column ($AaTir^{TIR}$ and $BtTir^{TIR}$) on a S200 HiLoad 26/600 column (BcThsA, AbThsA, EfThsA and SeThsA) pre-equilibrated with gel-filtration buffer. The peak fractions were analysed by SDS-PAGE, and the fractions containing $AaTir^{TIR}$, $BtTir^{TIR}$ or ThsA were pooled and concentrated to final concentrations of approximately 11.2 mg/mL ($AaTir^{TIR}$), 4.1 mg/mL ($BtTir^{TIR}$), 34.4 mg/mL (BcThsA), 46.2 mg/mL (AbThsA), 37.1 mg/mL (EfThsA) and 39.5 mg/mL (SeThsA), flash-frozen as 10 µL aliquots in liquid nitrogen, and stored at -80°C.

$BcThsA^{SLOG}$, $BcThsA^{SIR2}$ and $SeThsA^{SIR2}$: The cells were harvested by centrifugation at 5000 x *g* at 4°C for 15 min, the cell pellets were resuspended in 2-3 mL of lysis buffer (50 mM HEPES pH 8.0, 500 mM NaCl) per g of cells. The resuspended cells were lysed using a digital sonicator and clarified by centrifugation (15,000 x *g* for 30 minutes). The clarified lysate was supplemented with imidazole (final concentration of 30 mM) and then applied to a nickel HisTrap column (Cytiva) pre-equilibrated with 10 CVs of the wash buffer (50 mM HEPES pH 8.0, 500 mM NaCl, 30 mM imidazole) at a rate of 4 mL/min. The column was washed with 10 CVs of the wash buffer, followed by elution of bound proteins using elution buffer (50 mM HEPES pH 8, 500 mM NaCl, 250 mM imidazole). The elution fractions were analysed by SDS-PAGE and the fractions containing $BcThsA^{SLOG}$, $BcThsA^{SIR2}$ or $SeThsA^{SIR2}$ were pooled, supplemented with TEV protease and dialysed into gel-filtration buffer (10 mM HEPES pH 7.5, 150 mM NaCl) for 16-20 h. After dialysis, cleaved $BcThsA^{SLOG}$, $BcThsA^{SIR2}$ or $SeThsA^{SIR2}$ was reloaded onto the HisTrap column to remove the TEV protease, His_6-tag and contaminants. After the second IMAC step, $BcThsA^{SLOG}$, $BcThsA^{SIR2}$ or $SeThsA^{SIR2}$ were further purified on a S200 HiLoad 26/600 column pre-equilibrated with gel-filtration buffer. The peak fractions were analysed by SDS-PAGE, and the fractions containing $BcThsA^{SLOG}$, $BcThsA^{SIR2}$ or $SeThsA^{SIR2}$ were pooled and concentrated to final concentrations of approximately 49 mg/ml ($BcThsA^{SLOG}$), 8.3 mg/mL ($BcThsA^{SIR2}$), and 32 mg/mL ($SeThsA^{SIR2}$), flash-frozen as 10 µL aliquots in liquid nitrogen, and stored at -80°C.

AbTir, BXY39700, BtTir, Bovatus_RS22005, AMN69_RS28245, DORFOR_RS09155, PROVRUST_05034, AMN69_RS06490, CLOBOL_01188 for HPLC assays: expression vectors were transformed into *E. coli* (NEB Iq/LysY, catalog number 3013I). Single colonies were grown overnight in LB with kanamycin, diluted 100x in LB, and shaken at 30°C to mid-exponential phase (OD 0.4-0.8). Protein expression was induced by adding IPTG to a final concentration of 0.1 mM and shaking at 30°C for 3 hours. Cultures were pelleted by centrifugation then resuspended in binding buffer (100 mM Tris HCl, 150 mM NaCl, pH 8.0). 10x protease inhibitor cocktail was added, samples were lysed by sonication, and lysates were clarified by ultracentrifugation. 200 µL of streptactin magnetic bead suspension (PureCube-HiCap Streptactin MagBeads, Cube Biotech), washed three times with binding buffer, was suspended with each lysate sample and incubated for 1 h at 4°C with gentle agitation. Protein-laden beads were washed three times with binding buffer and resuspended in 200 µL of binding buffer.

$ROQ1^{TIR}$, $L6^{TIR}$ and $RUN1^{TIR}$ were produced as described previously (*13, 48*).

Fluorescence-based NADase assay

1, N^6-ethenoNAD (εNAD) (Sigma-Aldrich), a fluorescent analog of NAD^+, was used as the substrate in this assay (*13, 59*). The assay was carried out in 96-well microplate (Greiner). Fluorescence intensity was measured using a CLARIOstar® microplate reader (excitation wavelength 310-330 nm; emission wavelength 390-410 nm; readings every 1-3 minutes over 4 hours at 25 °C). The change in fluorescence over time was calculated from the slopes of the linear component of the curves. For all the fluorescence-based NADase assays, 100 µM protein and 100 µM substrate were used. The data was analyzed by Microsoft Excel and Prism GraphPad.

NAD$^+$-cleavage product quantification by HPLC

In vitro reactions consisted of 10 µL of protein-laden bead suspension and 40 µL of 10 µM NAD$^+$ in 25 mM HEPES buffer (pH 7.5) at room temperature with constant agitation. Reactions were quenched at 1 h or 48 h by pulling the beads to the side and transferring 40 µL of the reaction mixture to a new tube containing 160 µL of ice-cold 0.5 M $HClO_4$. Acid metabolite extracts were spun at 20,400 x *g* for 10 minutes at 4°C. 150 µL of supernatant were neutralized with 16 µL of 3 M K_2CO_3 and again spun at 20,400 x *g* for 10 min at 4°C. 90 µL of supernatant were mixed with 10 µL 0.5 M potassium phosphate buffer. Metabolites were analyzed by HPLC (Shimadzu LC40) using a C18 analytical column (Kinetex, 100 x 3 mm, Phenomenex).

NMR-based NADase assay

NMR samples were prepared in 175 µL HBS buffer (50 mM HEPES, 150 mM NaCl, pH 7.5), 20 µL D_2O, and 5 µL DMSO-d6, resulting in a total volume of 200 µL. Each sample was subsequently transferred to a 3 mm Bruker NMR tube rated for 600 MHz data acquisition. All ^1H NMR spectra were acquired with a Bruker Avance 600 MHz NMR spectrometer equipped with $^1H/^{13}C/^{15}N$ triple resonance cryoprobe at 298 K. To suppress resonance from H_2O, a water-suppression pulse program (P3919GP), using a 3-9-19 pulse-sequence with gradients (*60, 61*), was implemented to acquire spectra with an acquisition delay of 2 s and 32 scans per sample. For each reaction, spectra were recorded at 10 min, 2 h, 4 h, 8 h, 16 h, 40 h, and 64 h time-points, depending on instrument availability. All spectra were processed by TopSpin™ (Bruker) and Mnova 11 (Mestrelab Research). The amount of NAD$^+$ consumption was calculated based on the integration of non-overlapping resonance peaks, which vary depending on sample composition, from NAD$^+$ and nicotinamide, respectively. The detection limit (signal-to-noise ratio > 2) was estimated to be 10 µM. NAD$^+$ consumption is reported in a percentage range from -10% to 110%, to account for imprecise NMR measurements due to intrinsic fluctuations of the magnetic environment, especially at the first time-point of data acquisition.

STD-NMR

Samples for STD-NMR were prepared in similar solutions as for NMR NADase asasys. With a total volume of 200 µL, each sample consisted of 175 µL HBS buffer, 20 µL D_2O, and 5 µL DMSO-d6. STD-NMR spectra were acquired with Bruker Avance 600 MHz NMR spectrometer. The pulse-sequence STDDIFFGP19.3, in-built within the TopSpin™ program (Bruker), was employed to acquire STD-NMR spectra (*62*). This pulse-sequence consists of a 3-9-19 water-suppression pulse, the parameters of which were obtained from the water-suppression pulse program (P3919GP), to suppress the resonance from H_2O. The on-resonance irradiation was set close to protein resonances at 0.8 ppm, whereas the off-resonance irradiation was set far away from any protein or ligand resonances at 300 ppm. A relaxation delay of 4 s was used, out of which a saturation time of 3 s was used to irradiate the protein with a train of 50 ms Gaussian shaped pulses. The number of scans was 512. All spectra were processed by TopSpin™ (Bruker) and Mnova 11 (Mestrelab Research).

Production and purification of v-cADPR and v2-cADPR

Production reactions for v-cADPR and v2-cADPR were performed using conditions similar to the ^1H NMR NADase assays. Each reaction was carried out in HBS buffer (50 mM HEPES, 150 mM NaCl, pH 7.5). For v-cADPR production, 1 µM of His_6-tagged $AbTir^{TIR}$, and 10 mM NAD$^+$ were added to the mixture. For v2-cADPR production, 10 µM of His_6-tagged $AaTir^{TIR}$, and 20 mM NAD$^+$ were added to the mixture. All reactions were performed at room temperature and

monitored intermittently by ^{1}H NMR. To stop the reaction, the His_6-tagged protein was removed by incubating the mixture with 200 mL of HisPur™ Ni-NTA resin for 30-60 min. The resin was subsequently removed by centrifugation at 500 x *g* for 1 min and the supernatant was subjected to HPLC-based separation to purify the products. A Shimadzu Prominence HPLC equipped with a Synergi™ 4 µm Hydro-RP 80 Å column was used for separation. The mobile phase consisted of phase A (0.05 % (v/v) formic acid in water) and phase B (0.05 % (v/v) formic acid in methanol). Different gradients, flow rates, and run times were applied, depending on prior optimization with individual reaction mixtures. Product peaks were confirmed by comparison with individual chromatograms of NAD^+, nicotinamide and ADPR. Fractions corresponding to the product peaks were collected, concentrated, and lyophilized and stored at −20°C. For v2-cADPR production by HopAM1 in plants, HopAM1 was transiently expressed in *N. benthamiana* leaves in an estradiol-inducible plant binary vector. *N. benthamiana* leaves were ground with a mortar and pestle in liquid nitrogen. The ground powders were resuspended in 10 mL of 50% methanol kept at -40 °C and then mixed with 10 mL chloroform at −40°C. Samples were then centrifuged at 15,000 x *g* for 10 min at 0 °C and the aqueous/methanol layer was removed. The extract was lyophilized and stored at −80°C until HPLC. The v2-cADPR was purified by manual fractionation with HPLC.

NMR structure determination of cADPR isomers

Purified v-cADPR and v2-cADPR were used to determine their structures. At the Griffith University facility, 4 mg of v-cADPR and 4.9 mg of v2-cADPR were dissolved in 560 µL of D_2O, respectively. Each sample was transferred to a 5 mm NMR tube rated for 600 MHz. The Bruker Avance 600 MHz NMR spectrometer was utilized to acquire ^{1}H, ^{13}C, ^{1}H -^{1}H COSY, ^{1}H-^{13}C HSQC, and ^{1}H-^{13}C HMBC spectra at 298 K. The chemical structure of each compound was determined by assignments of ^{1}H and ^{13}C peaks and correlations, especially those linking two ribose rings (Fig. 1, Table S2-3). In addition, ^{1}H-^{31}P HMBC spectrum was acquired for a sample of 2'cADPR with a Bruker 400 MHz NMR spectrometer. At the University of Warwick facility, samples were dissolved in D_2O and ^{1}H, COSY, HSQC, HMBC, NOESY spectra were acquired on Bruker Avance II 700 MHz spectrometer equipped with TCI cryoprobe. The sample was also used to acquire ^{1}H-^{31}P HMBC on a Bruker 600 MHz spectrometer with a BBO probe. All experiments were done at 25 °C. At the University of Nebraska-Lincoln facility, HopAM1-produced v2-cADPR was purified by HPLC, lyophilized, and reconstituted in 160 µL of deuterium oxide and transferred into a 3-mm NMR tube. The samples were analyzed with a Bruker Avance-III HD 700 MHz NMR system equipped with a 5 mm QCI-P cryoprobe or a Bruker Avance NEO 600 MHz NMR system equipped with a TCI-H/F cryoprobe. The chemical structure of the compound was determined by assignment of 1- and 2-dimensional NMR data, including ^{1}H, ^{13}C, ^{1}H-^{1}H COSY, NOESY, ^{1}H-^{13}C HSQC, ^{1}H-^{13}C HMBC, ^{1}H-^{13}C HSQC-TOCSY, and ^{1}H-^{31}P HSQC-TOCSY (Table S4).

LC-MS/MS analysis

A Waters Xevo TQXS triple quadruple mass spectrometer coupled with Waters I-class UPLC was used for LC-MS/MS analysis of v-cADPRs from both *in vitro* products of AbTir and AaTir NAD^+ activity and plant compounds extracted in 10% methanol, 1% acetic acid. The mass spectrometer is equipped with an electrospray ionization source in positive ion mode. Source condition: capillary voltage: 800 V, desolvation temperature: 600°C, desolvation gas: 1000 L/h, congas: 150 L/h and nebuliser gas: 7 bar. MRM transitions for v-cADPRs are parent ions at m/z 542.00 and daughter ions at 136.00 and 348.02, with collision energy at 32 and 28 eV, respectively. UPLC mobile phases comprised A: water with 2 mM ammonium acetate; and B: 100% methanol.

The elution gradient was: 0-5 min, 100% A, 5-7 min, 80% A, 7-8 min, 100% B, then isocratic for 2 min at 100% B before equilibrating back to 100% A for 15 min. Flow rate was set at 0.2 mL/min. The column used was a Waters Acquity UPLC CSH C18, 1.7 μm, 0.1x100 mm. High-resolution measurements were done on a Bruker MaXis II Q-TOF mass spectrometer.

Size-exclusion chromatography (SEC)-coupled multi-angle light scattering (MALS)

A DAWN HELEOS II 10-angle light-scattering detector coupled with an Optilab rEX refractive index detector (Wyatt Technology), combined with a Superdex 200 5/150 Increase size exclusion column (Cytiva), connected to a Prominence HPLC (Shimadzu), was used for SEC-MALS. The column was equilibrated in gel-filtration buffer, and 30 μL of the purified proteins were run through the column at 0.25 mL/min. Molecular masses were calculated using Astra 6.1 (Wyatt Technology).

Isothermal titration calorimetry (ITC)

ITC experiments were performed in duplicate on Nano ITC (TA Instruments). All proteins and compounds were dissolved in a buffer containing 10 mM HEPES (pH 7.5) and 150 mM NaCl. The baseline was equilibrated for 600 s before the first injection. 0.3 mM v-cADPR (2'cADPR) or v2-cADPR (3'cADPR) was titrated as 30 injections of 1.44 μL every 200 s into 50-112.4 μM AbThsA, or 20 injections of 1.44 μL every 200 s into 24-37 μM EfThsA. The heat change was recorded by injection over time and the binding isotherms were generated as a function of molar ratio of the protein solution. The dissociation constant (K_d) values were obtained after fitting the integrated and normalized data to a single-site binding model using NanoAnalyze (TA Instruments).

Protein crystallization

$AbTir^{TIR}$ crystals were obtained using the hanging-drop vapour diffusion method. Initial trays were set up using the mosquito® crystallization robot (SPT Labtech). Several initial hits were obtained within a day in different commercial crystallization screens (Hampton Research Index Screen (HR2-144), Molecular Dimensions JCSG-plus Screen (MD1-37) and Molecular Dimensions SG1 Screen (MD 1-88)). Diffraction-quality crystals of $AbTir^{TIR}$ were produced using 0.1 M Bis-Tris pH 5.5, 0.2 M $LiSO_4$, and 25% PEG 3350 at 20°C. EasyXtal 15-Well Tool (Qiagen) was used for the optimization of the crystals.

$BtTir^{TIR}$: Diffraction-quality crystals were grown by the hanging drop vapour diffusion method at 293 K, with drops containing 1 μL of protein (20 mg/mL), and 1 μL of reservoir solution (0.1 M Hepes pH 7.0, 0.2 M $MgCl_2$ and 16-22% PEG 3350); they appeared within a week.

$BcThsA^{SLOG}$:3'cADPR: Diffraction-quality crystals were grown by the hanging drop vapour diffusion method at 293 K, with drops containing 1 μL of protein (10 mg/mL) with 1 mM 3'cADPR, and 1 μL of reservoir solution (0.1 M Bis-Tris pH 5.5, 0.1 M ammonium sulfate and 25-29% PEG 3350); they appeared within a week.

SeThsA: Diffraction-quality crystals were grown by the hanging drop vapour diffusion method at 293 K, with drops containing 1 μL of protein (5.5 mg/mL), and 1 μL of reservoir solution (0.1 M Mes pH 6.0, 0.2 M potassium sodium tartrate tetrahydrate and 28-30% PEG smear low (*63*)); they appeared within a week.

Crystallographic data collection

$AbTir^{TIR}$: The crystals were harvested using 18 mm Mounted CryoLoop™ - 20 micron (Hampton) and cryoprotected using 50% well solution + 30% PEG 400 or 50% well solution +

30% glycerol. The harvested crystals were immediately flash-cooled in liquid nitrogen. X-ray diffraction data were collected using a wavelength of 0.9537 Å at the Australian Synchrotron MX2 beamline. Diffraction data were collected using the Blu-Ice software and indexed and integrated using XDS (*64*). Data scaling was done with Aimless in the CCP4 suite (*65*). Crystal structures were solved by molecular replacement with Phaser (*66*), using $TcpB^{TIR}$ (PDB: 4LQC) as the search model. Model building and structure refinement were performed using Coot (*67*) and Phenix-refine (*66*), respectively. Data processing and refinement statistics are given in Table S5.

$BtTir^{TIR}$: The crystals were cryoprotected in 20% glycerol and flash-cooled at 100 K. X-ray diffraction data were collected from single crystals on the MX2 beamline at the Australian Synchrotron, using a wavelength of 0.9537 Å. The datasets were processed using XDS (*64*) and scaled using Aimless in the CCP4 suite (*65*). The structure was solved by molecular replacement using Phaser (*68*) and the $AbTir^{TIR}$ structure as the template. The models were refined using Phenix (*69*), and structure validation was performed using MolProbity (*70*). Data processing and refinement statistics are given in Table S5.

$BcThsA^{SLOG}$:3'cADPR: The crystals were cryoprotected in 20% glycerol and flash-cooled at 100 K. X-ray diffraction data were collected from single crystals on the MX2 beamline at the Australian Synchrotron, using a wavelength of 0.9537 Å. The datasets were processed using XDS (*64*) and scaled using Aimless in the CCP4 suite (*65*). The structure was solved by molecular replacement using Phaser (*68*) and the SLOG domain of the BcThsA crystal structure (PDB: 6LHX) as the template (*23*). The models were built and refined using Phenix (*69*) and Coot, and structure validation was performed using MolProbity (*70*). Data processing and refinement statistics are given in Table S5.

SeThsA: The crystals were cryoprotected in 20% glycerol and flash-cooled at 100 K. X-ray diffraction data were collected from single crystals on the MX2 beamline at the Australian Synchrotron, using a wavelength of 0.9537 Å. The datasets were processed using Mosflm (*71*) and scaled using Aimless in the CCP4 suite (*65*). The structure was solved by molecular replacement using Phaser (*68*) and an AlphaFold2 (*72*) model of SeThsA as the template. The models were built and refined using Phenix (*69*), Coot and ISOLDE (*73*) and structure validation was performed using MolProbity (*70*). Data processing and refinement statistics are given in Table S5.

Electron microscopy

Negative-stain electron microscopy: After dilution, $AbTIR^{TIR}$ (at 5 mg/mL) was incubated with 2 mM **3AD** at 25°C for 1 h. Protein was diluted to 0.1 mg/mL in gel filtration buffer (containing 30 mM HEPES, pH 7.5, and 150 mM NaCl) and 2 mM **3AD,** before being loaded onto grids. 6 µL sample was placed on a carbon-coated copper gird and incubated for 5 min. The grid was then washed with gel filtration buffer containing 2 mM **3AD**, stained with 2% uranyl acetate for 30 s and air-dried. The images were collected on the Hitachi HT7700 120 kV transmission electron microscope at 25,000x magnification at 120 keV.

Cryo-EM sample preparation and data collection: $AbTir^{TIR}$ was diluted to 5 mg/mL and incubated with 2 mM **3AD** at 25°C for 1 h. Protein was then diluted to 2.5 mg/mL with gel filtration buffer containing 2 mM **3AD**, before being loaded onto grids. Quantifoil Au R 1.2/1.3 300 mesh holey carbon girds were glow-discharged for 30 s at medium level after 1 min evacuation of both carbon and copper sides. A volume of 2 µL of sample solution was added to the grids, and samples were vitrified in a Leica EMGP2 plunge freezer using a blotting time of 8.5 s at 8°C, with 96% humidity. Screening and data collection were performed on a JEOL Cryo-ARM300 operated at 300 keV and equipped with an in column Ω energy filter (slit width 20 eV) and Gatan K3 direct electron detector. Cryo-EM data collection settings are summarized in Table S6.

Cryo-EM data processing and 3D reconstruction: all data processing was performed with cryoSPARC (*74*); the cryo-EM processing workflow is summarized in Fig. S5. Filaments were auto-picked using filament tracer in cryoSPARC. Several rounds of 2D classification were performed to remove inferior particles. After 2D classification, good particles were further classified into three 3D maps using ab initio reconstruction. The best reconstruction was used as a reference for helical refinement. After several rounds of helical refinement and CTF refinement, the final resolution of the 3D reconstruction is 2.74 Å.

Model building and refinement: The crystal structure of $AbTir^{TIR}$ was docked into the electrostatic potential map in ChimeraX (*75*) and fit using ISOLDE (*73*). **3AD** and structurally different regions were manually built or adjusted in ISOLDE and Coot (*67*). Models were refined using multiple rounds of phenix.real_space_refine (*76*).

Generation of transgenic *Arabidopsis thaliana*

Transgenic *Arabidopsis thaliana* plants were generated by floral-dipping transformation with *Agrobacterium tumefaciens* (*77*). Briefly, *A. thaliana* inflorescences were dipped with *Agrobacterium tumefaciens* strains carrying pER8-HopAM1 or $HopAM1^{E191A}$ resuspended in a 5% sucrose solution containing 0.02% Silwet L-77. The transformed plants were maintained till maturity in a micro-climate-controlled growth chamber at 24 °C, with a 10 h light/14 h dark cycle. Seeds were collected and transformants were selected on MS medium with hygromycin (10 mg/mL) and validated by PCR and immunoblot.

Phytobacterial challenges

Five-week old *Arabidopsis thaliana* Col-0 grown under short days (8 h light, 16 h dark, 120 microeinsteins, 65% relative humidity) were challenged with *Pseudomonas syringae* pv. tomato strain DC3000 or its 28 effector-deleted derivative (D28E) at OD_{600nm} of 0.15 and left for 18 h under lights. Challenged leaves were harvested 18 h later, snap-frozen in liquid nitrogen and freeze-dried. Samples were processed for LC-MS/MS as described previously (*54*).

ROS assay

ROS production was determined as described previously (*78*). Briefly, transgenic *Arabidopsis* leaves were sprayed with 20 µM estradiol containing 0.02% Silwet-L77. After 24 hours, leaf discs were excised using a 4 mm diameter cork borer and incubated in H_2O in white 96-well microtiter plates overnight. The H_2O was then replaced with 0.5 mM luminol-based chemiluminescent probe L-012 and 1 mM flg22 in 10 mM MOPS-KOH buffer (pH 7.4). The production of ROS was determined by counting photons using with a Synergy 5 luminometer (BioTek, Winooski, VT, USA).

In vivo chemiluminescence imaging

4-5 week-old *FRK1-LUC* plants (*36, 37, 79*) were sprayed with 1 mM D-luciferin (Sigma) in 0.01% w/v Triton X-100 and incubated in the dark for 30 min, before challenge with DC3000 or DC3000*ΔhopAM1-1/1-2*. Luciferase images were acquired in a dark box at room temperature using a Retiga R6 CCD camera (Qimaging) with a 25 mm/f 2.5 Navitar lens. Photons were counted every 10 min at 2X2 binning mode and images processed using ImageJ.

Chlorophyll fluorescence

Photosystem II chlorophyll fluorescence imaging of pathogen-challenged Arabidopsis rosettes was performed with a CF Imager (Technologica Ltd, Colchester, UK). Dark-adapted (20

min) plants were inoculated. Maximum dark-adapted fluorescence (F_m) was determined by treating with a saturating light pulse (6,349 µmol $m^{-2}s^{-1}$ for 0.8 s) followed by actinic light (120 µmol $m^{-2}s^{-1}$ – the same as standard plant growth conditions) for 15 min, then a saturating pulse to obtain maximum light adapted fluorescence ($F_{m'}$). The plants remained in actinic light for a further 24 min, followed by a dark period of 20 min. This cycle (59 min duration) was repeated 23 times and F*v*/F*m* calculated as described previously (*80*).

Production of 2',3'-cAMP/cGMP by HopAM1

His-tagged HopAM1 protein was purified using CelLytic B kit (Sigma-Aldrich) and HIS-Select Nickel Affinity Gel (Sigma-Aldrich) according to manufacturer's specifications. The purified His-tagged HopAM1 protein was incubated with 100 ng lambda DNA overnight, and the products detected by HPLC. Transgenic Arabidopsis expressing HopAM1 were sprayed with 20 µM estradiol containing 0.02% Silwet-L77. After 24 hours, whole leaves were detached, ground with liquid nitrogen, and metabolites were extracted using 250 µL 50% MeOH and 250 µL chloroform. Metabolites were analyzed by HPLC alongside 2',3'-cAMP/cGMP standards (BIOLOG Life Science Institute).

Bioinformatic analysis

To identify positions important for determining the product specificity of TIR domain NADases, we aligned 278 TIR-domain sequences using HMM (hidden Markov model). Positions where >20% of the sequences contained gaps relative to the HMM profile to which they were aligned were excluded (110 out of 116 positions were kept). Additionally, sequences that lacked significant similarity to the profile were removed (bitscore <0), as were sequences that contained many gaps relative to the model (gaps at >15% of the 110 positions). The trimmed and filtered alignment yielded 267 TIR domain sequences and 110 positions (Data S1-S4); the alignment was subsequently used to calculate the mutual information (MI) (i) between TIR domains that possessed cyclase activity and those that produced ADPR, and (ii) among TIR domains that produced different forms of cADPR. The position corresponding to W204 in AbTir was identified as being highly informative (MI in 90th percentile) for cyclase activity, with the second lowest MI of all positions when calculating MI between TIR domains making the three different cyclic products (cADPR, v-cADPR and v2-cADPR), behind only the catalytic glutamate.

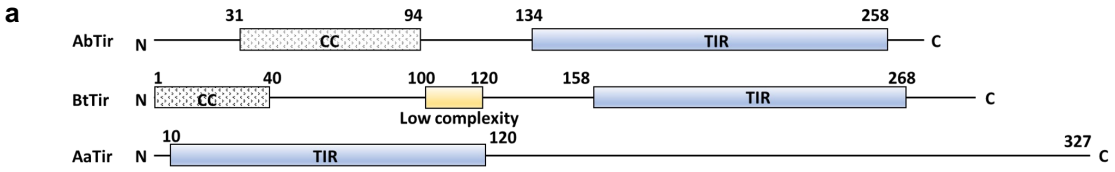
a
AbTir
N
31
94
CC
134
258
TIR
C
BtTir
1
40
100
120
158
268
Low complexity
AaTir
10
120
327

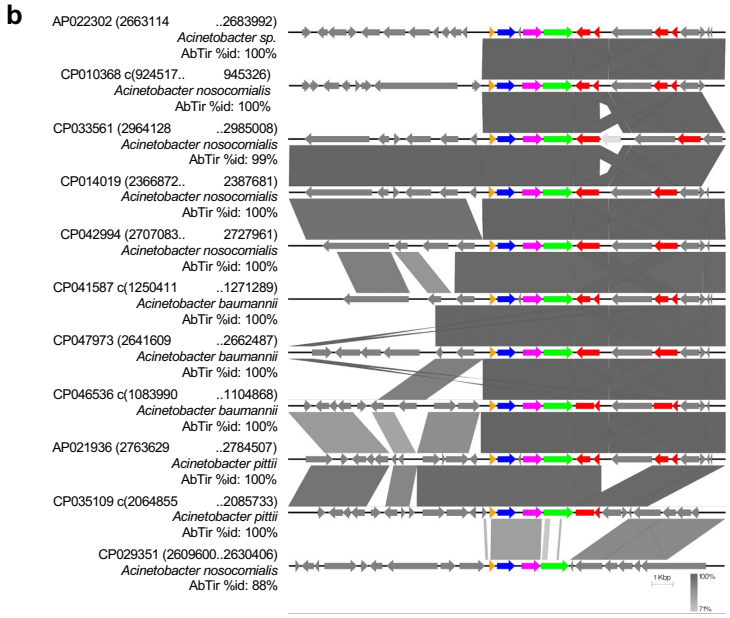
b
AP022302 (2663114 ..2683992)
Acinetobacter sp.
AbTir %id: 100%
CP010368 c(924517.. 945326)
Acinetobacter nosocomialis
AbTir %id: 100%
CP033561 (2964128 ..2985008)
Acinetobacter nosocomialis
AbTir %id: 99%
CP014019 (2366872.. 2387681)
Acinetobacter nosocomialis
AbTir %id: 100%
CP042994 (2707083.. 2727961)
Acinetobacter nosocomialis
AbTir %id: 100%
CP041587 c(1250411 ..1271289)
Acinetobacter baumannii
AbTir %id: 100%
CP047973 (2641609 ..2662487)
Acinetobacter baumannii
AbTir %id: 100%
CP046536 c(1083990 ..1104868)
Acinetobacter baumannii
AbTir %id: 100%
AP021936 (2763629 ..2784507)
Acinetobacter pittii
AbTir %id: 100%
CP035109 c(2064855 ..2085733)
Acinetobacter pittii
AbTir %id: 100%
CP029351 (2609600..2630406)
Acinetobacter nosocomialis
AbTir %id: 88%

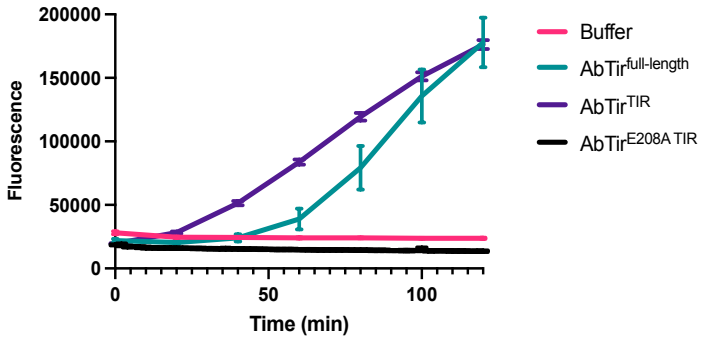
c
Fluorescence
200000
150000
100000
50000
0
0
50
100
Time (min)
Buffer
AbTir full-length
AbTir TIR
AbTir E208A TIR

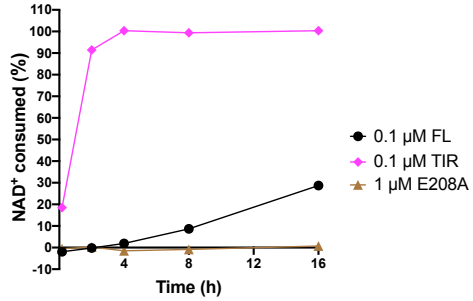
d
NAD+ consumed (%)
110
100
90
80
70
60
50
40
30
20
10
0
-10
4
8
12
16
Time (h)
0.1 μM FL
0.1 μM TIR
1 μM E208A

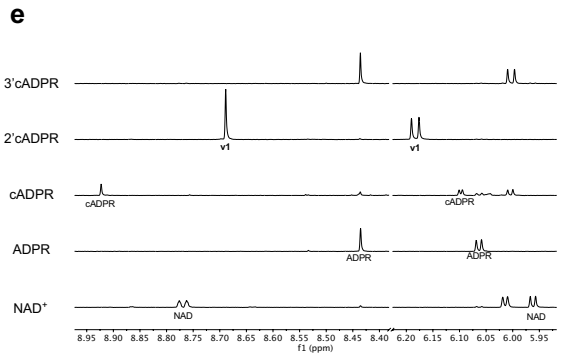
e
3'cADPR
2'cADPR
cADPR
ADPR
NAD+
v1
cADPR
ADPR
NAD
8.95 8.90 8.85 8.80 8.75 8.70 8.65 8.60 8.55 8.50 8.45 8.40 6.20 6.15 6.10 6.05 6.00 5.95
f1 (ppm)

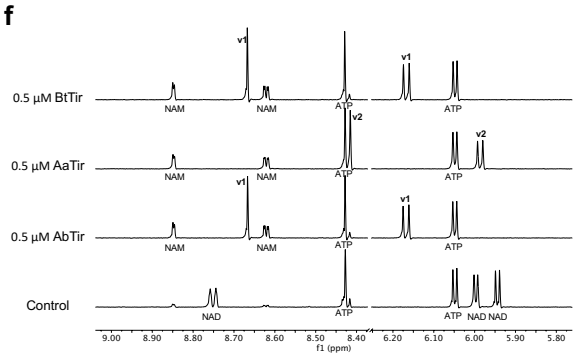
f
0.5 μM BtTir
0.5 μM AaTir
0.5 μM AbTir
Control
v1
v2
NAM
ATP
NAD
9.00 8.90 8.80 8.70 8.60 8.50 8.40 6.20 6.10 6.00 5.90 5.80
f1 (ppm)

Fig. S1. Genomic location and enzymatic characterization of AbTir. (a) Schematic diagram of the domain organization of AbTir, BtTir, and AaTir. CC, coiled coil domain; TIR, Toll/interleukin-1 receptor (TIR) domain. (b) Pairwise sequence comparison of 10 kilobases up- and down-stream of the gene encoding AbTir. Greyscale bars represent the level of nucleotide sequence identity for that region, as indicated by the scale. Sequence annotations are colour-coded by function: blue, AbTir; orange, integrase; pink, chromate resistance; green, chromate transporter; red, IS*3* family insertion sequence; salmon, other insertion sequence; and grey, other/unknown function. We identified AbTir in 11 complete *Acinetobacter* genomes; in each case, AbTir was located between an integrase gene and two genes encoding chromate resistance and transporter proteins, which are adjacent to 0-2 copies of an insertion sequence belonging to the IS*3* family. (c) NADase activity of $AbTir^{full\text{-}length}$, TIR domain, CC domain and the catalytic glutamate mutant of the TIR domain. Data are presented as mean ± SD (n = 3). (d) ^{1}H NMR assay showing different NADase activities for wild-type $AbTir^{full\text{-}length}$ (FL), wild-type $AbTir^{TIR}$ and $AbTir^{TIR\_E208A}$. (e) Expansions of ^{1}H NMR spectra comparing selected peaks of purified NAD^+, ADPR, cADPR, 2'cADPR (v1), and 3'cADPR. Concentration was 500 μM for all compounds and spectra were acquired in the same environment (solvent and temperature) as for NMR NADase assays. Unique peaks for each compound were labelled. Although peaks shown for 3'cADPR are not unique and overlap with peaks from NAD^+ (~6.02 ppm) and ADPR (~8.44 ppm), 3'cADPR can be easily identified with the absence of other NAD^+ and/or ADPR peaks. (f) Expansions of ^{1}H NMR spectra showing the absence of new peaks (products) for NADase assays in the presence of ATP. NAD^+ was cleaved into nicotinamide (NAM) and either 2'cADPR (v1) for AbTir and BtTir or 3'cADPR (v2) for AaTir. No change was observed for ATP signals. Initial concentrations for NAD^+ and ATP were both 1 mM, and 10 mM $MgCl_2$ was also present in all samples. Incubation time was 40 h.

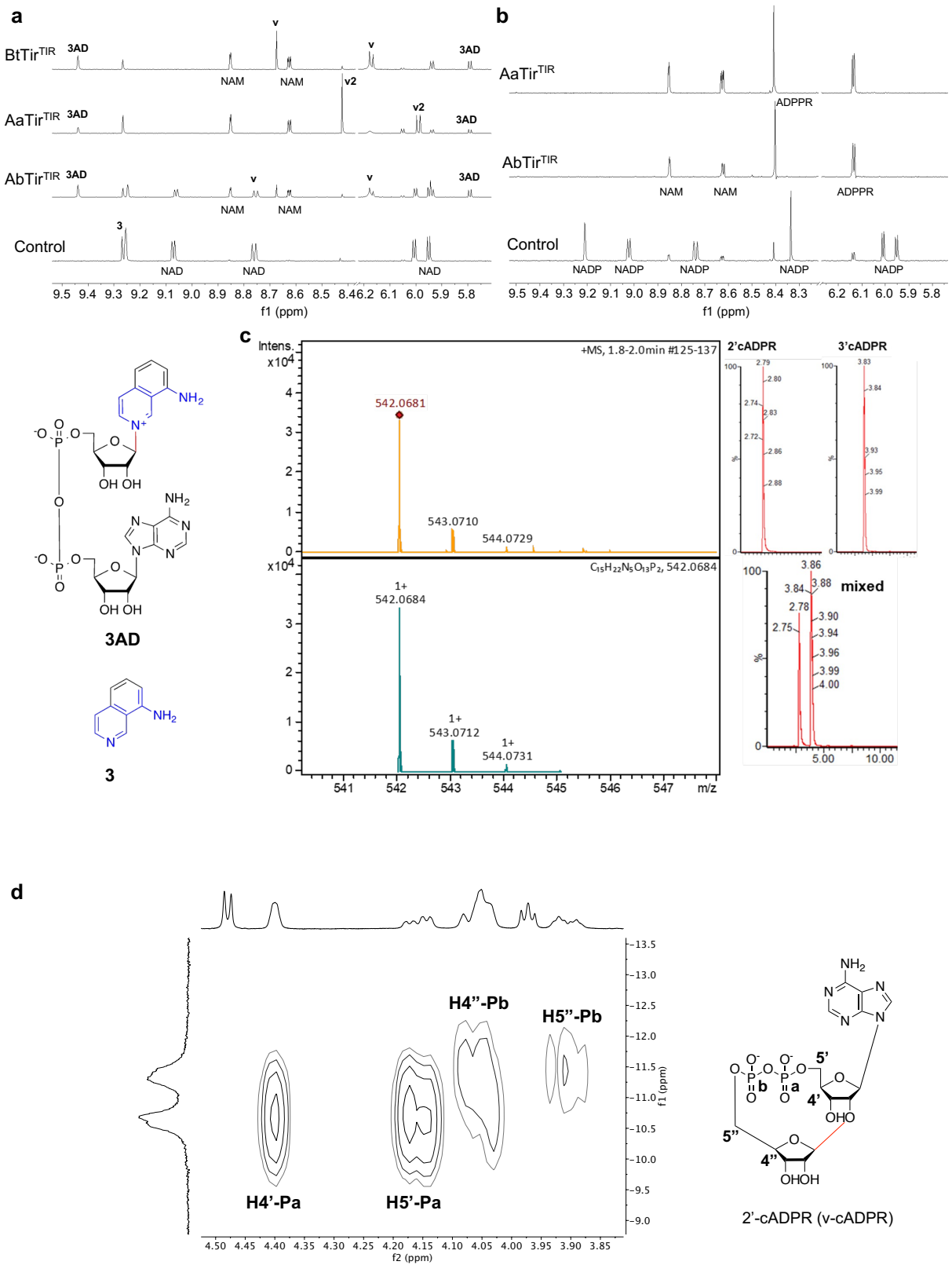
a
BtTir^TIR
AaTir^TIR
AbTir^TIR
Control
3AD
NAM
v
v2
3
NAD
f1 (ppm)
b
AaTir^TIR
AbTir^TIR
Control
ADPPR
NADP
f1 (ppm)
3AD
3
c
Intens.
+MS, 1.8-2.0min #125-137
542.0681
543.0710
544.0729
C15H22N5O13P2, 542.0684
1+
542.0684
543.0712
544.0731
m/z
2'cADPR
3'cADPR
mixed
d
H4"-Pb
H5"-Pb
H4'-Pa
H5'-Pa
f2 (ppm)
f1 (ppm)
2'-cADPR (v-cADPR)

Fig. S2. NMR and MS analyses of cADPR isomers. (a) Expansions of ^{1}H NMR spectra, showing base-exchange reactions by 0.1 μM AbTir^{TIR}, 0.5 μM AaTir^{TIR} and 2.5 μM BtTir^{TIR}. The initial concentration for both NAD^{+} and **3** (8-amino-isoquinoline) was 500 μM. Spectra for AbTir^{TIR} and BtTir^{TIR} correspond to 40 h incubation time, while for AaTir^{TIR} the incubation time was 16 h. Selected peaks are labelled, showing the formation of base-exchange product **3AD** for both proteins, as well as the production of v-cADPR (2'cADPR) (v) and v2-cADPR (3'cADPR) (v2). (b) Expansions of ^{1}H NMR spectra showing hydrolysis of NADP to nicotinamide and ADPPR by AbTir^{TIR} and AaTir^{TIR}. The initial concentration of NADP was 500 μM, while the protein concentration was 0.5 μM. All spectra correspond to 16 h incubation time. Selected peaks are labelled. (c) LC-MS/MS of the 2'cADPR and 3'cADPR isomers produced by AbTir^{TIR} and AaTir^{TIR} NADase activity, respectively. (Left) High-resolution mass spectrum of AbTir^{TIR} 2'cADPR. Top; measured spectrum, bottom; simulated spectrum. (Right) LC-MS/MS of AbTir^{TIR} and AaTir^{TIR} reveal the distinct 2'cADPR and 3'cADPR isomers. (d) ^{1}H-^{31}P HMBC of v-cADPR (2'cADPR).

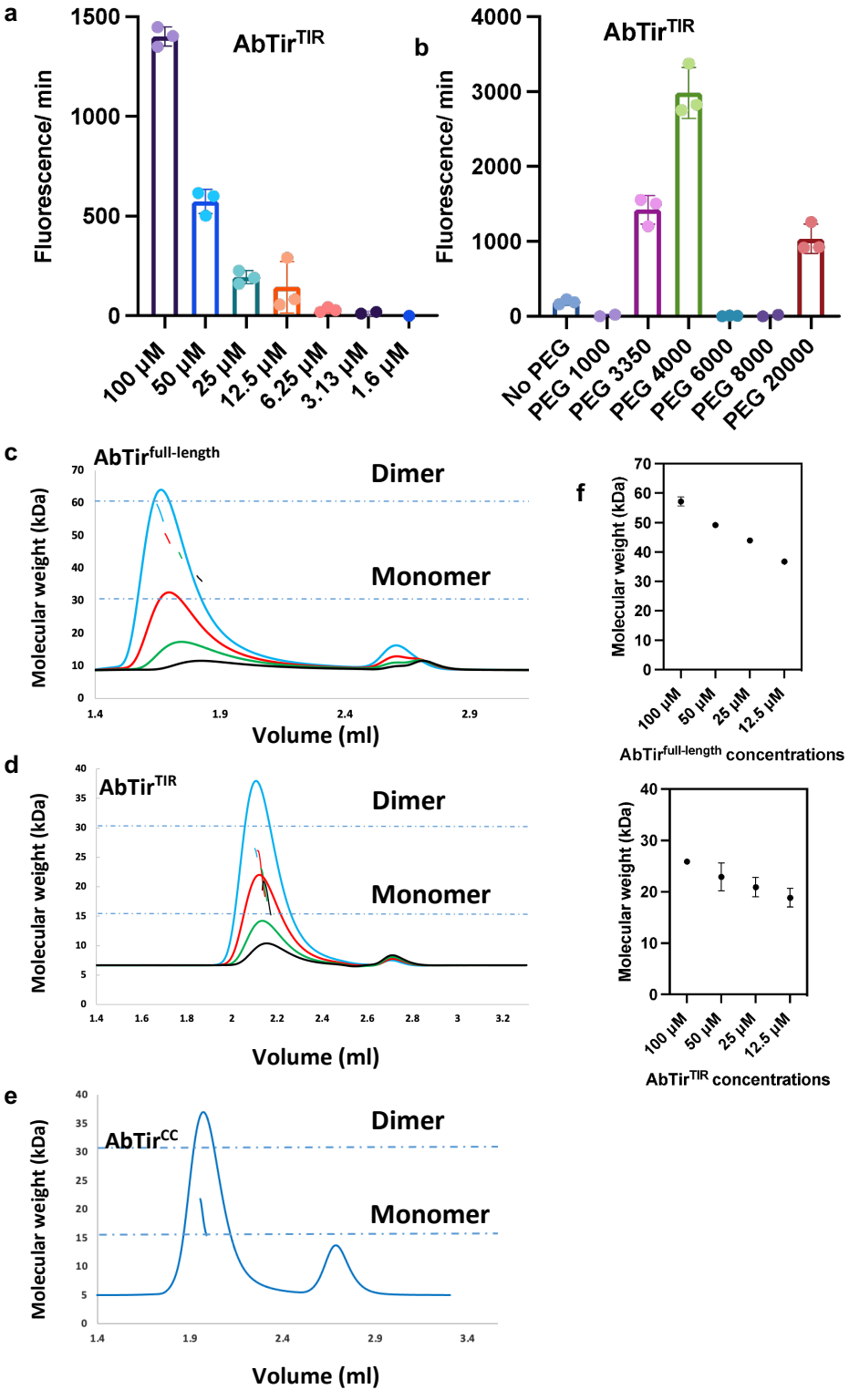
a
AbTir^TIR
Fluorescence/ min
1500
1000
500
0
100 µM
50 µM
25 µM
12.5 µM
6.25 µM
3.13 µM
1.6 µM
b
AbTir^TIR
Fluorescence/ min
4000
3000
2000
1000
0
No PEG
PEG 1000
PEG 3350
PEG 4000
PEG 6000
PEG 8000
PEG 20000
c
AbTir^full-length
Dimer
Monomer
Molecular weight (kDa)
Volume (ml)
d
AbTir^TIR
Dimer
Monomer
Molecular weight (kDa)
Volume (ml)
e
AbTir^CC
Dimer
Monomer
Molecular weight (kDa)
Volume (ml)
f
Molecular weight (kDa)
100 µM
50 µM
25 µM
12.5 µM
AbTir^full-length concentrations
Molecular weight (kDa)
100 µM
50 µM
25 µM
12.5 µM
AbTir^TIR concentrations

Fig. S3. Self-association is required for the enzymatic activity of AbTir. (a) NADase activity of AbTir^{TIR} at different concentrations, measured by the fluorescence assay using εNAD. Data are presented as mean ± SD (n = 3). (b) Effect of macromolecular crowding agents in the enzymatic activity, measured by the fluorescence assay using εNAD. In this experiment, 25 μM AbTir^{TIR} and 20% PEG were used. Data are presented as mean ± SD (n = 3). (c) Size-exclusion chromatography-coupled multi-angle light scattering (SEC-MALS) analysis of AbTir$^{full-length}$ (1-269). The elution of the protein from the SEC column (Superdex 200) was measured as a direct refractive index (dRI). (d) SEC-MALS analysis of AbTir^{TIR} (134-269) on a Superdex 75 column. (e) SEC-MALS analysis of AbTir^{CC} (27-118) on a Superdex 75 column. (f) Molecular weights of AbTir$^{full-length}$ and its TIR domain as a function of concentration. At high concentrations (100 μM), AbTir$^{full-length}$ exists as a dimer in solution, whereas the TIR domain exists in a rapid monomer-dimer equilibrium. Data are presented as mean ± SD (n = 3).

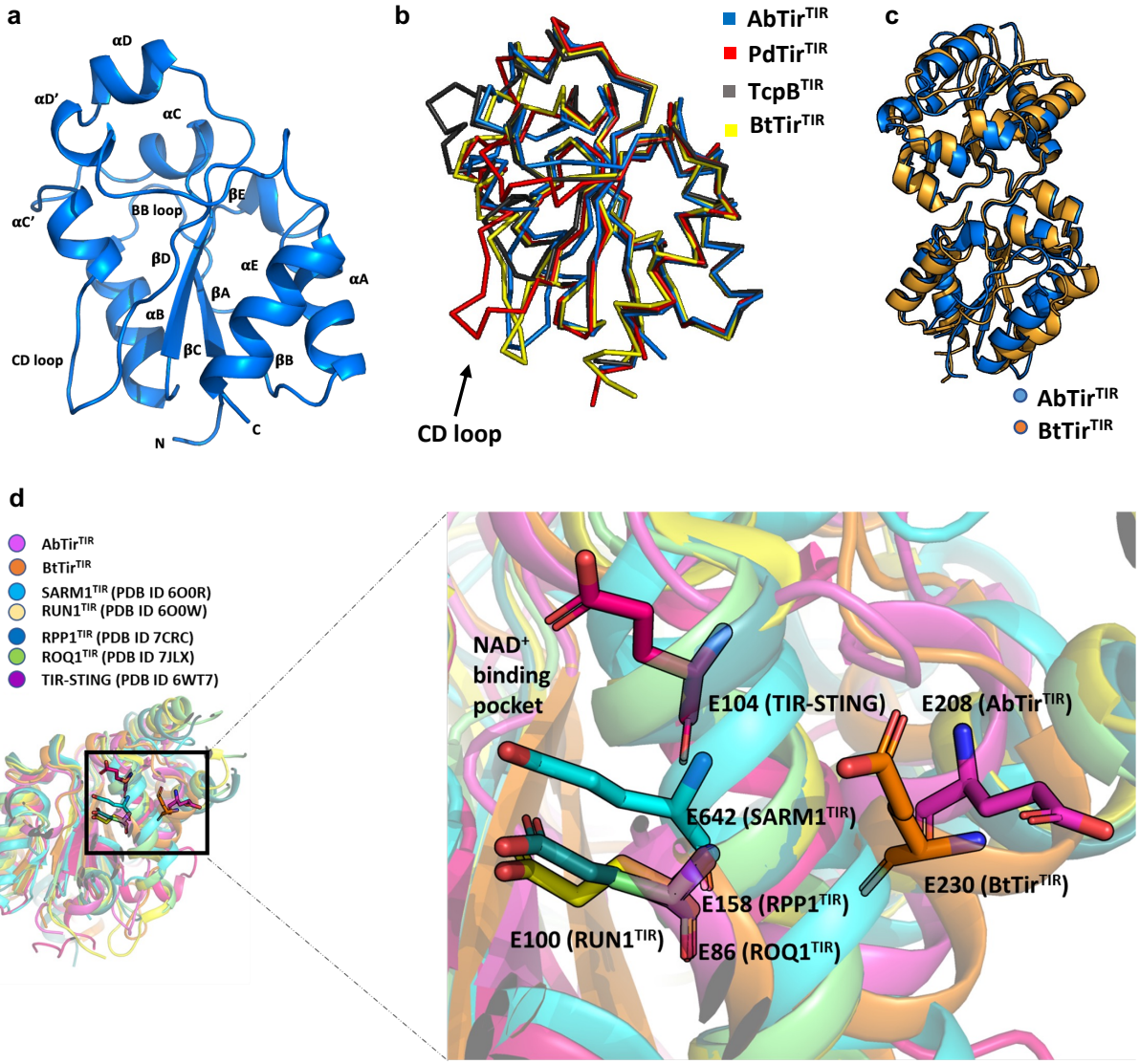
a
αD
αD'
αC
αC'
BB loop
βE
βD
αE
αA
βA
αB
CD loop
βC
βB
N
C
b
AbTir^TIR
PdTir^TIR
TcpB^TIR
BtTir^TIR
CD loop
c
AbTir^TIR
BtTir^TIR
d
AbTir^TIR
BtTir^TIR
SARM1^TIR (PDB ID 6O0R)
RUN1^TIR (PDB ID 6O0W)
RPP1^TIR (PDB ID 7CRC)
ROQ1^TIR (PDB ID 7JLX)
TIR-STING (PDB ID 6WT7)
NAD+ binding pocket
E104 (TIR-STING)
E208 (AbTir^TIR)
E642 (SARM1^TIR)
E230 (BtTir^TIR)
E158 (RPP1^TIR)
E100 (RUN1^TIR)
E86 (ROQ1^TIR)

Fig. S4. Crystal structures of AbTir^{TIR}and BtTir^{TIR}. (a) Crystal structure of AbTir^{TIR}. (b) Structural superposition of AbTir^{TIR} and BtTir^{TIR} with PdTir^{TIR} (PDB: 3H16) and TcpB^{TIR} (PDB: 4C7M). (c) Structural superposition of AbTir^{TIR} and BtTir^{TIR} homodimers observed in the crystal structure, coloured blue and orange, respectively. (d) Structural superposition of the catalytic glutamate of AbTir^{TIR} with other NAD+-consuming TIR domains.

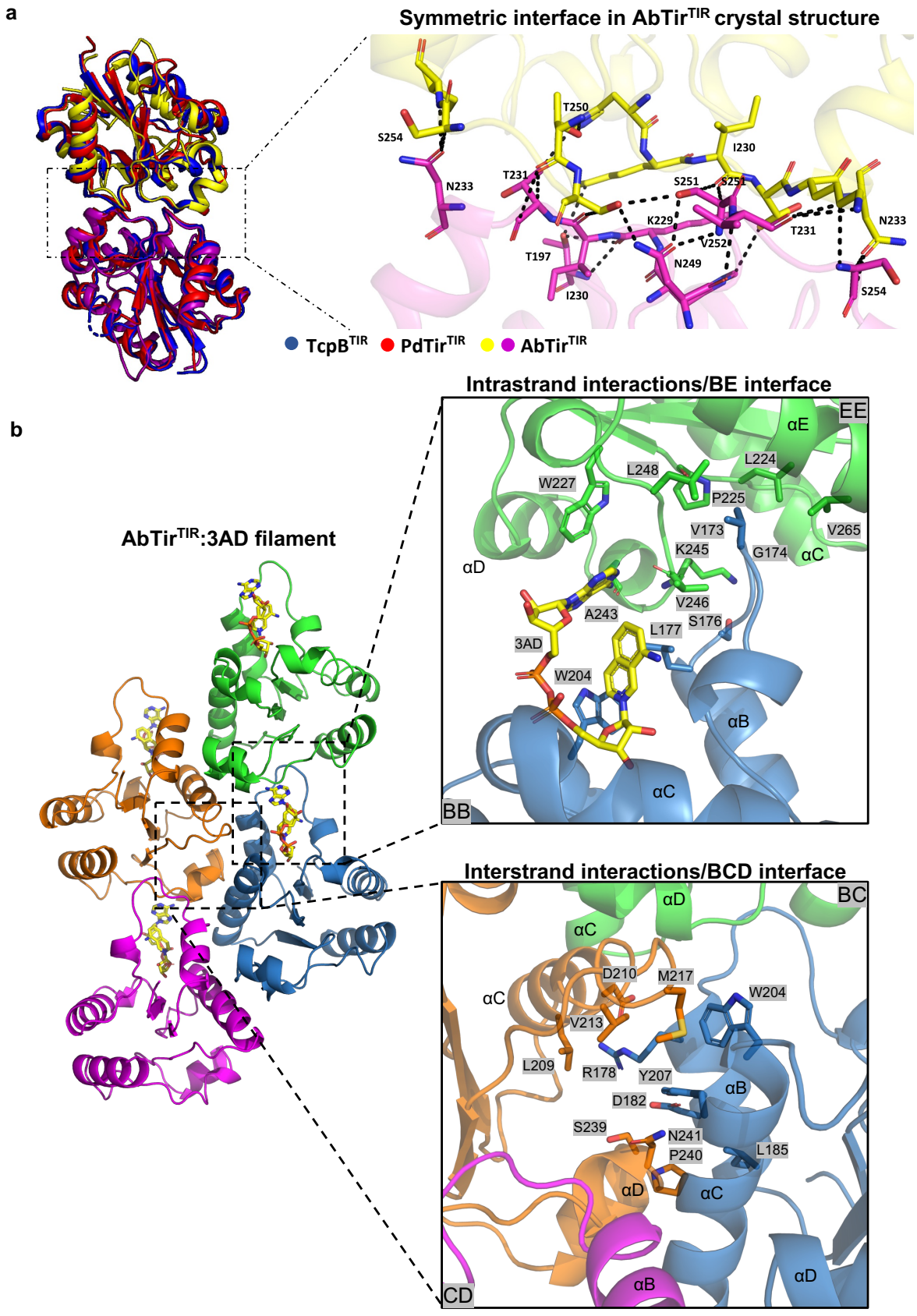
a
Symmetric interface in AbTir^TIR crystal structure
S254
N233
T250
I230
T231
S251
S251
K229
T231
N233
V252
T197
N249
I230
S254
TcpB^TIR
PdTir^TIR
AbTir^TIR
b
AbTir^TIR:3AD filament
Intrastrand interactions/BE interface
EE
αE
L224
L248
W227
P225
V173
V265
K245
G174
αC
αD
V246
A243
S176
L177
3AD
W204
αB
αC
BB
Interstrand interactions/BCD interface
BC
αD
αC
D210
M217
W204
αC
V213
L209
R178
Y207
αB
D182
S239
N241
L185
P240
αD
αC
αB
αD
CD

Fig. S5. Detailed interactions within the AbTir^{TIR} crystal and cryo-EM structures. (a) Left panel: Structural superposition of the symmetric dimer interface of AbTir^{TIR} with PdTir^{TIR} and TcpB^{TIR} (4LZP). The two molecules of AbTir^{TIR} are coloured green and cyan, respectively; the extra helix from the TcpB structure is removed for better comparison and visualization. Right panel: close-up view of the interacting residues of the symmetric dimer interface of AbTir^{TIR}. (b) Detailed interactions within the AbTir^{TIR}:**3AD** filament. BB surface consists of residues in the BB loop; EE surface consists of residues in βD and βE strands, and the αE helix; BC surface consists of residues in αB and αC helices; whereas CD surface consists of residues in the CD loop and the αD helical region.

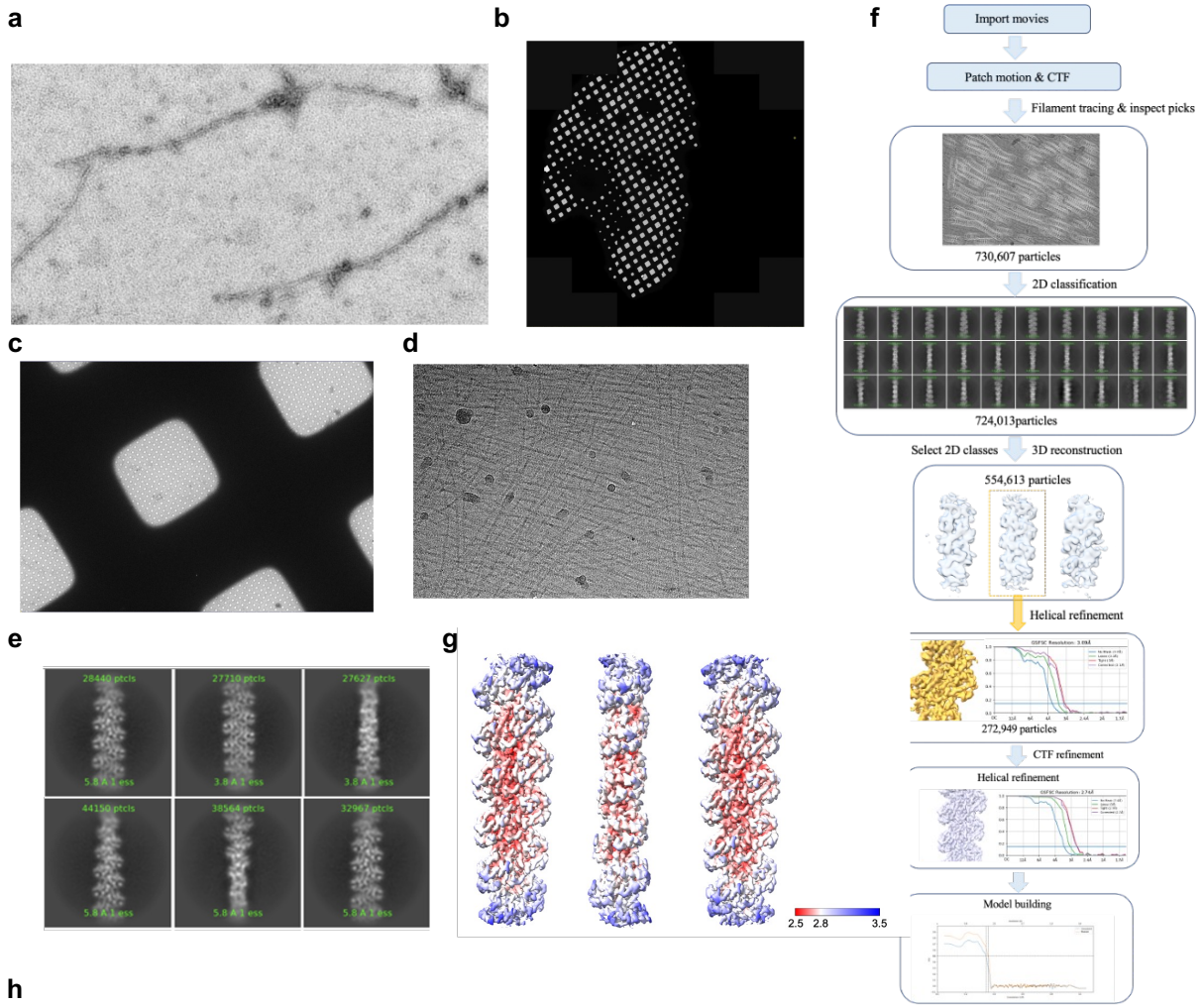
a
b
c
d
e
f
g
h
Import movies
Patch motion & CTF
Filament tracing & inspect picks
730,607 particles
2D classification
724,013particles
Select 2D classes
3D reconstruction
554,613 particles
Helical refinement
272,949 particles
CTF refinement
Helical refinement
Model building
2.5 2.8 3.5
Chain A
Chain A
Chain A
V173
K202
αB
αC
R186
N218
D234
E144
αA
αD
αE
D160
L267
3AD
Chain C
Chain C
Chain C
V173
K202
αB
αC
R186
N218
D234
E144
αA
αD
αE
D160
L267
3AD

Fig. S6. Structure determination of the AbTir^{TIR}:3AD complex by cryo-EM. (a) Negative-stain electron micrograph of AbTir^{TIR}:NAD^{+}. The magnification was 10,000x, and the grids were prepared as for AbTir^{TIR}:**3AD**). (b-d) Representative low and high magnification cryo-EM micrographs. (e) Representative 2D class averages. (f) Flow-chart of the cryo-EM processing steps, gold-standard FSC curves of the final 3D reconstruction, and map-to-model FSC curve of the final model and the the electrostatic potential density map. (g) Local-resolution distribution of the final map. (h) Representative regions of electrostatic potential maps for **3AD**-bound AbTir^{TIR}.

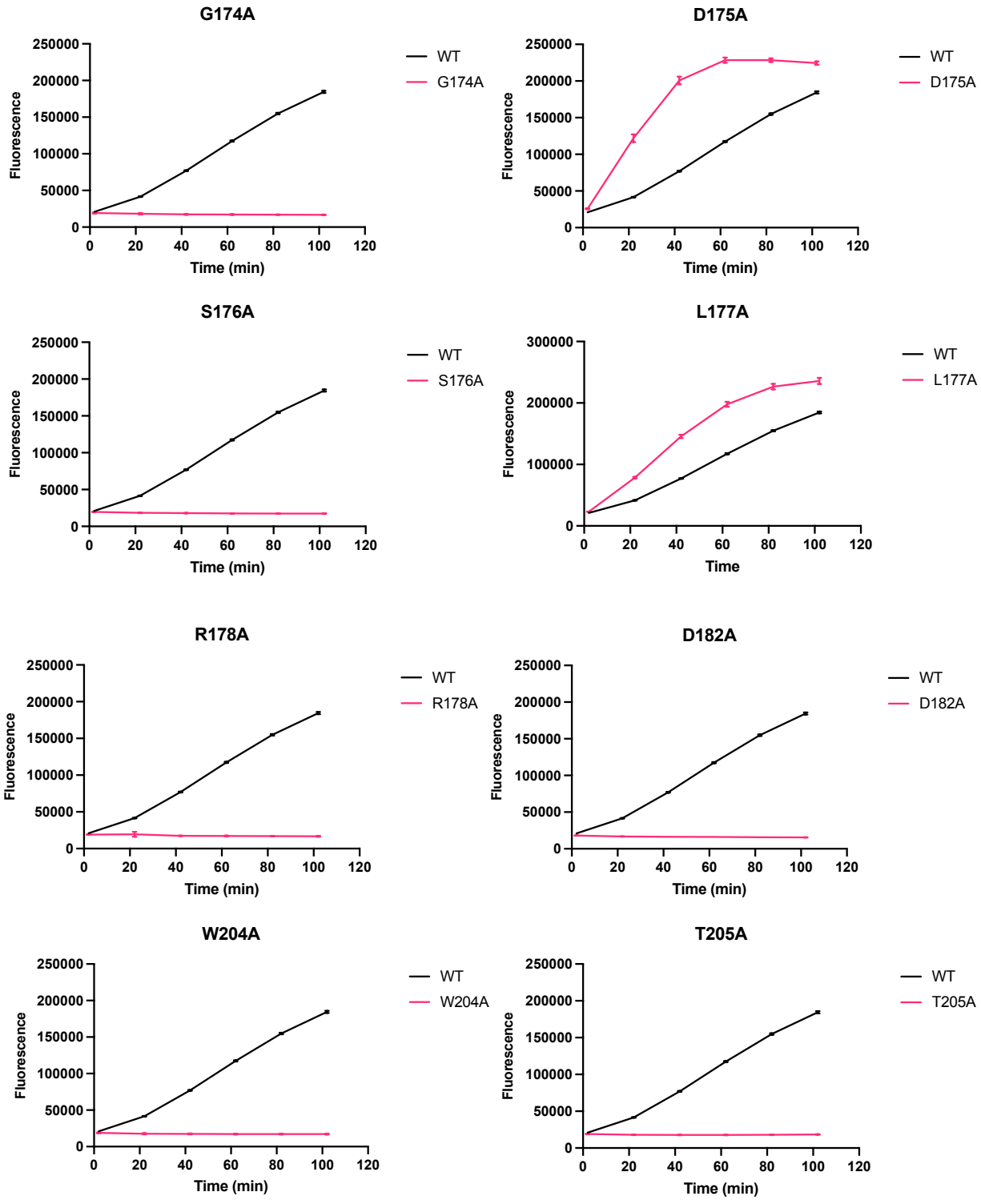
G174A
Fluorescence
Time (min)
WT
G174A
D175A
Fluorescence
Time (min)
WT
D175A
S176A
Fluorescence
Time (min)
WT
S176A
L177A
Fluorescence
Time
WT
L177A
R178A
Fluorescence
Time (min)
WT
R178A
D182A
Fluorescence
Time (min)
WT
D182A
W204A
Fluorescence
Time (min)
WT
W204A
T205A
Fluorescence
Time (min)
WT
T205A

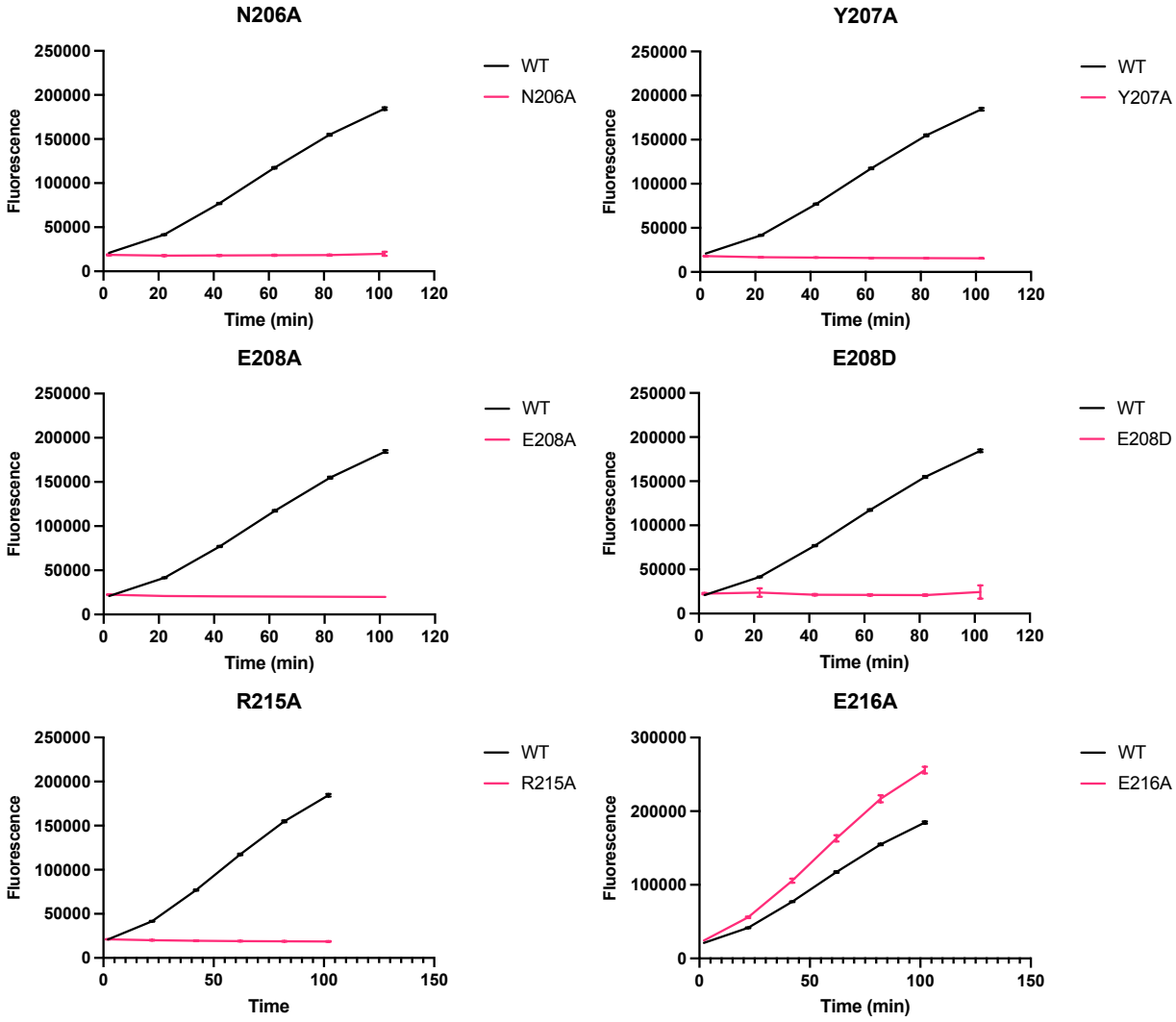
N206A
Fluorescence
Time (min)
WT
N206A
Y207A
Fluorescence
Time (min)
WT
Y207A
E208A
Fluorescence
Time (min)
WT
E208A
E208D
Fluorescence
Time (min)
WT
E208D
R215A
Fluorescence
Time
WT
R215A
E216A
Fluorescence
Time (min)
WT
E216A

Fig. S7. Time-courses of NADase assays for AbTir^{TIR} mutants. The assays were performed using 100 μM 1, N6 -ethenoNAD (εNAD) and 100 μM protein concentration; n = 3 for all groups. The D175A and L177A mutants show higher activity than the wild-type protein; the corresponding residues are part of the BB loop and mutation of these residues could modulate this loop to improve TIR-domain self-association and/or interaction with the substrate.

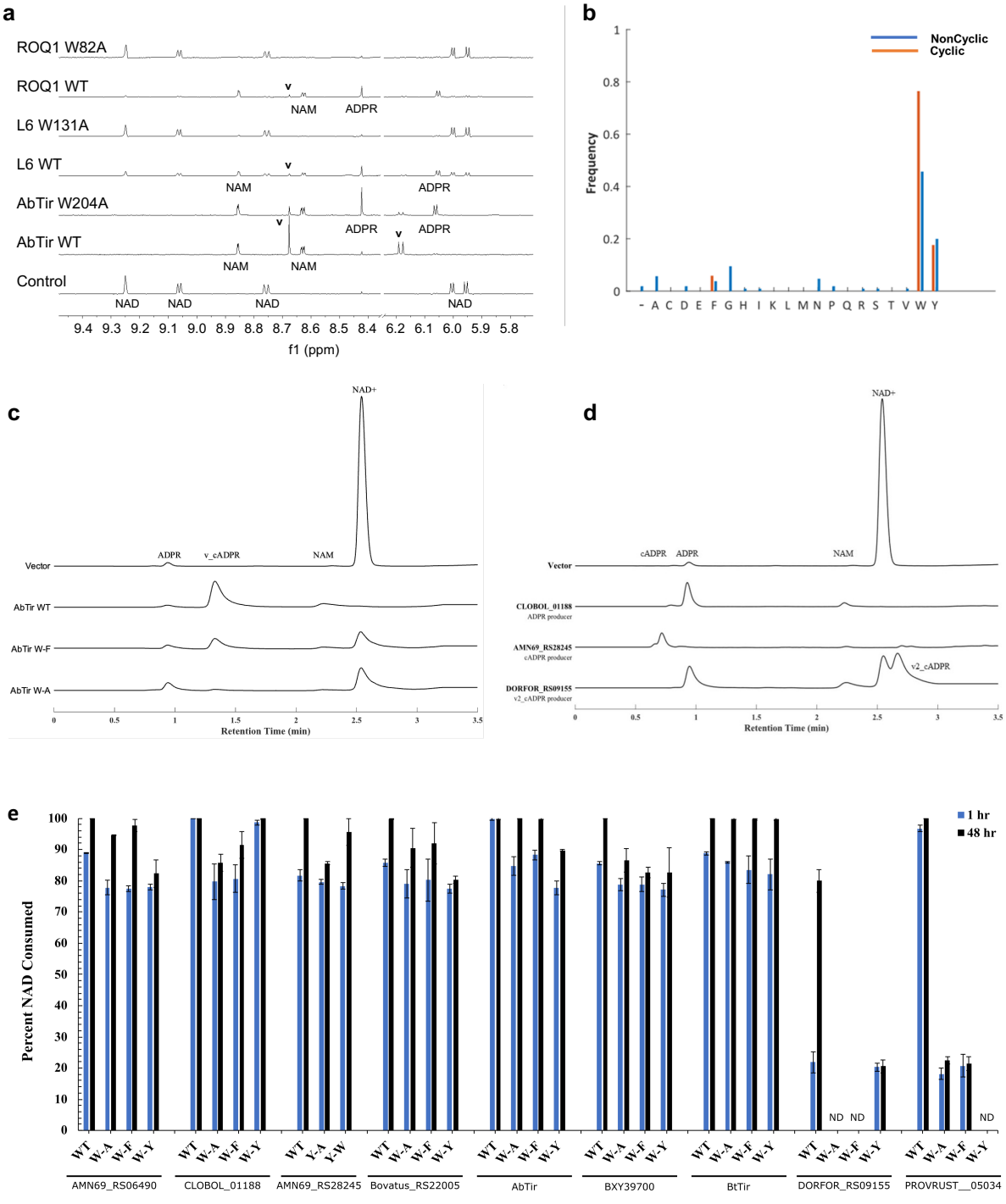
a
ROQ1 W82A
ROQ1 WT
NAM
ADPR
L6 W131A
L6 WT
AbTir W204A
AbTir WT
Control
NAD
9.4 9.3 9.2 9.1 9.0 8.9 8.8 8.7 8.6 8.5 8.4 6.2 6.1 6.0 5.9 5.8
f1 (ppm)
b
NonCyclic
Cyclic
Frequency
- A C D E F G H I K L M N P Q R S T V W Y
c
NAD+
ADPR
v_cADPR
NAM
Vector
AbTir WT
AbTir W-F
AbTir W-A
Retention Time (min)
d
NAD+
cADPR
ADPR
NAM
Vector
CLOBOL_01188
ADPR producer
AMN69_RS28245
cADPR producer
DORFOR_RS09155
v2_cADPR producer
v2_cADPR
Retention Time (min)
e
Percent NAD Consumed
1 hr
48 hr
ND
WT W-A W-F W-Y
AMN69_RS06490
CLOBOL_01188
AMN69_RS28245
Bovatus_RS22005
AbTir
BXY39700
BtTir
DORFOR_RS09155
PROVRUST__05034

Fig. S8. Conserved tryptophan is essential for ADPR cyclization. (a) Expansions of ^{1}H NMR spectra, showing altered NADase activity for AbTir^{TIR} W204A, and absence of NADase activity for L6 W131A and ROQ1 W82A. The protein concentration was 50 μM for AbTir^{TIR} and 100 μM for L6^{TIR} and ROQ1^{TIR}, while the initial NAD^+ concentration was 500 μM. Spectra correspond to 24 h incubation time for AbTir^{TIR} samples and 16 h incubation time for L6^{TIR} and ROQ1^{TIR} samples. Selected peaks are labelled, showing the production of v-cADPR (v), nicotinamide, and ADPR with wild-type proteins but not mutants. (b) Frequencies of amino-acids observed at the position equivalent to AbTir W204 in a multiple sequence alignment of 122 functionally characterized TIR domains. Each bar represents the frequency of the indicated amino acid among TIR domains that do (cyclic, red) or do not (non-cyclic, blue) produce a cylic NAD^+ catabolite, i.e. cADPR, v-cADPR (2'cADPR) or v2-cADPR (3'cADPR). (c-d) HPLC chromatograms of NAD^+ consumption by different bacterial TIR domains. (c) HPLC chromatograms of metabolite extracts from wild-type and mutant AbTir^{TIR} reactions at 1 h. (d) HPLC chromatograms of metabolite extracts from various TIR domain (Table S1) reactions, illustrating the variety of NAD^+ catabolites. (e) Percent of starting NAD^+ consumed by wild-type and mutant TIR domains. Data are shown at 1 h and 48 h; n = 3 for all groups except where no data (ND) could be collected (presented as mean ± SD).

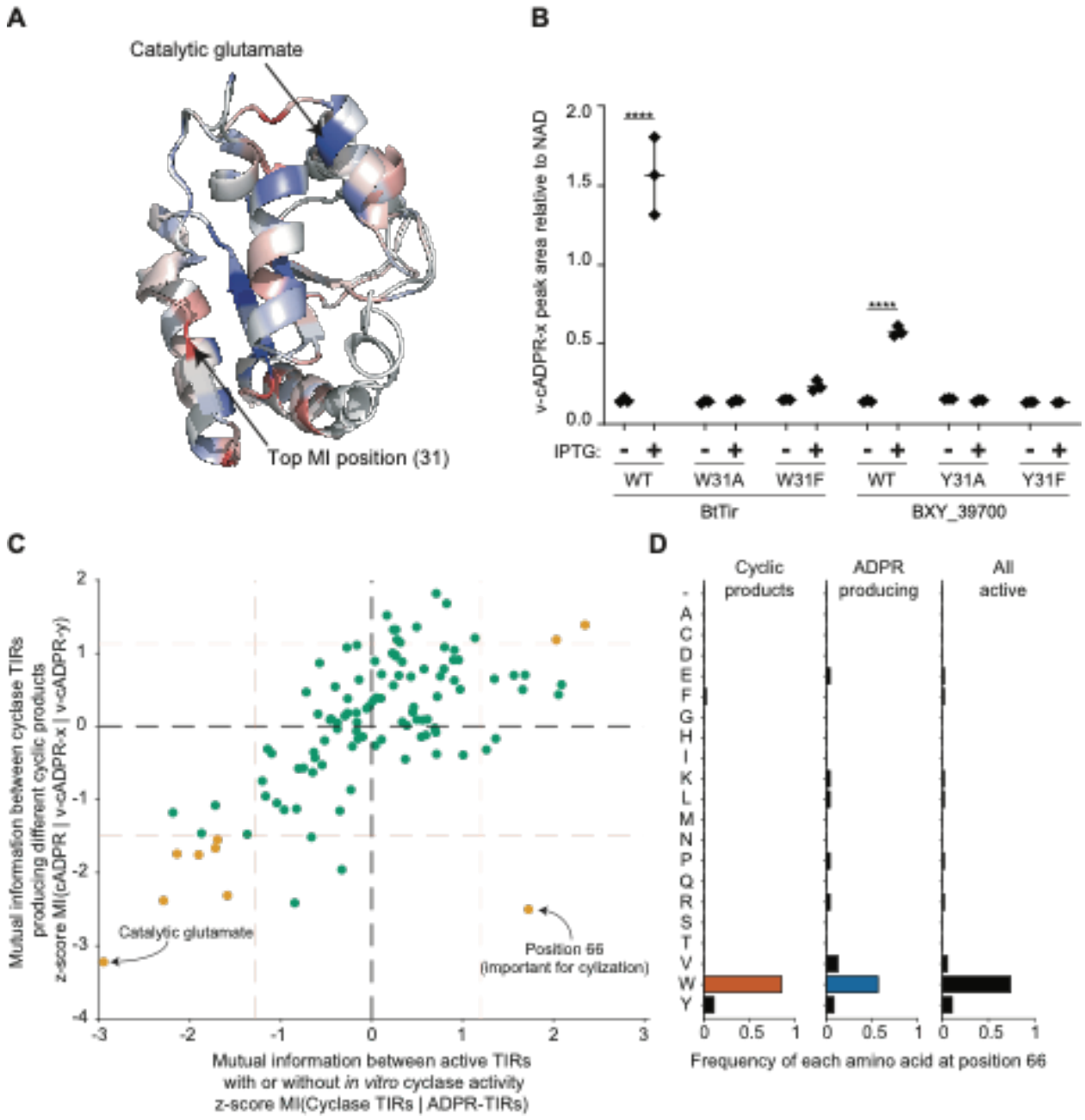
A
Catalytic glutamate
Top MI position (31)
B
v-cADPR-x peak area relative to NAD
2.0
1.5
1.0
0.5
0.0
****
****
IPTG: - + - + - + - + - + - +
WT
W31A
W31F
WT
Y31A
Y31F
BtTir
BXY_39700
C
Mutual information between cyclase TIRs producing different cyclic products
z-score MI(cADPR | v-cADPR-x | v-cADPR-y)
Catalytic glutamate
Position 66
(important for cyclization)
Mutual information between active TIRs with or without in vitro cyclase activity
z-score MI(Cyclase TIRs | ADPR-TIRs)
D
Cyclic products
ADPR producing
All active
A C D E F G H I K L M N P Q R S T V W Y
Frequency of each amino acid at position 66

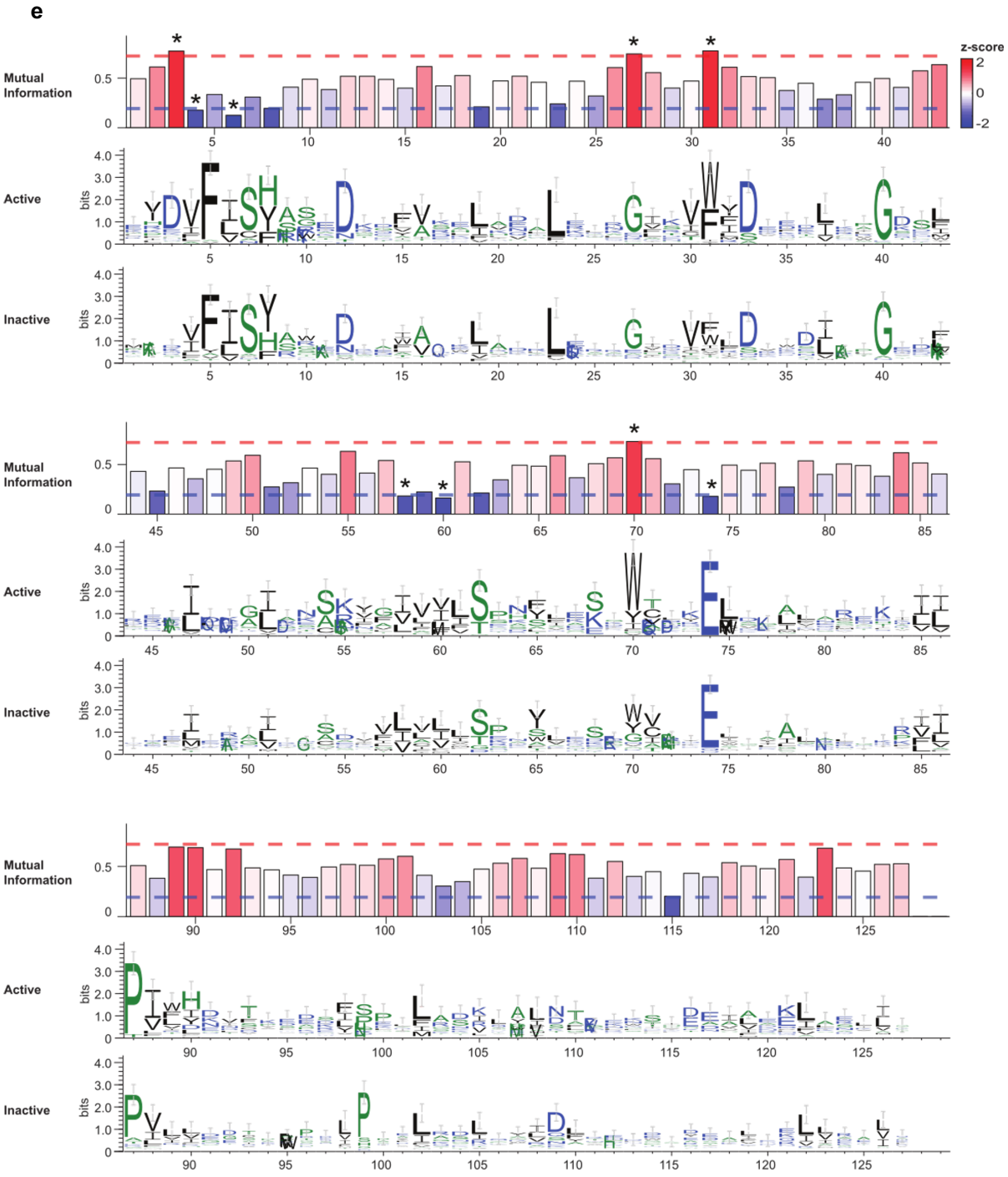
e
Mutual Information
Active
Inactive
bits
z-score
2
0
-2

Fig. S9. Mutual information analysis of TIR domains with, or without, NADase activity *in vitro*. (a) Mutual information (MI) between 'active' (NADase-positive) and 'inactive' (NADase-negative) TIR domains (n = 40 and n = 70, respectively) illustrated on the superimposed ribbon structures of the v-cADPR (2'cADPR)-producing TIR domains from *Bacteroides xylanisolvens* XB1A and *Bacteroides thetaiotaomicron* 7330. These structures were modeled using TcpB from *Brucella melitensis* ATCC 23457 (PDB: 4LZP) as the template. Structures are coloured based on the z-scored MI at each position, with red indicating positions that are most informative in delineating active from inactive TIR domains, and blue being the least informative. The top MI position (residue 31; tryptophan (W) in *B. thetaiotaomicron* 7330 and tyrosine (Y) in *B. xylanisolvens* XB1A), and the previously reported catalytic glutamate are shown. (b) Mutations at the position with the highest MI between active and inactive TIR domains in the v-cADPR (2'-cADPR) producing TIR domains from *B. thetaiotaomicron* 7330 (BtTir) and *B. xylanisolvens* XB1A (BXY_39700). The peak area of v-cADPR (2'-cADPR) was normalized to the peak area of NAD^+ measured in *E. coli* expressing wild-type (WT) and mutant TIR domains after a 1 h incubation in the presence or absence of the IPTG inducer of TIR expression (n=3; presented as mean ± SD). Note that endogenous NAD^+ in *E. coli* served as the substrate for the TIR domains. (c) Scatter-plot illustrating the relationship between positional MI calculated on an expanded set of TIR-domain sequences (267 sequences, 110 positions following filtering) comparing (i) active TIR domains with or without *in vitro* cyclase activity [z-score MI(cyclase TIR domains | ADPR-TIRdomains)] on the x-axis and (ii) between cyclase TIR domains producing different cyclic products [z-score MI (cADPR | v-cADPR | v2-cADPR)] on the y-axis. Points corresponding to positions where the calculated MI was in the bottom or top 10th percentile (dashed red lines) for both sets of comparisons are coloured in gold. The catalytic glutamate, which is fixed in both groups of sequences (MI = 0, lowest MI-Z-score) and position 66 in quadrant IV (corresponding to high MI between cyclase and ADPR-producing TIR domains and very low MI among TIR domains that make different cyclic products) are both labeled. (d) Frequency of each amino acid at position 66 of the filtered alignment within sequences that produced cyclic products, ADPR, or all active sequences. (e) MI identifies positions of importance to TIR enzymatic activity. MI calculated at 110 conserved positions in a multiple sequence alignment of TIR domains with and without cyclase activity. Bars are coloured by the z-score of the MI. Red and blue dashed lines indicate MI thresholds (top and bottom 10th percentile, respectively) used to identify residues that are important for TIR enzymatic activity. Sequence logos were generated from the multiple sequence alignment used to calculate MI between TIR domains that produced cyclic (n = 35) or non-cyclic (n = 23) products *in vitro*.

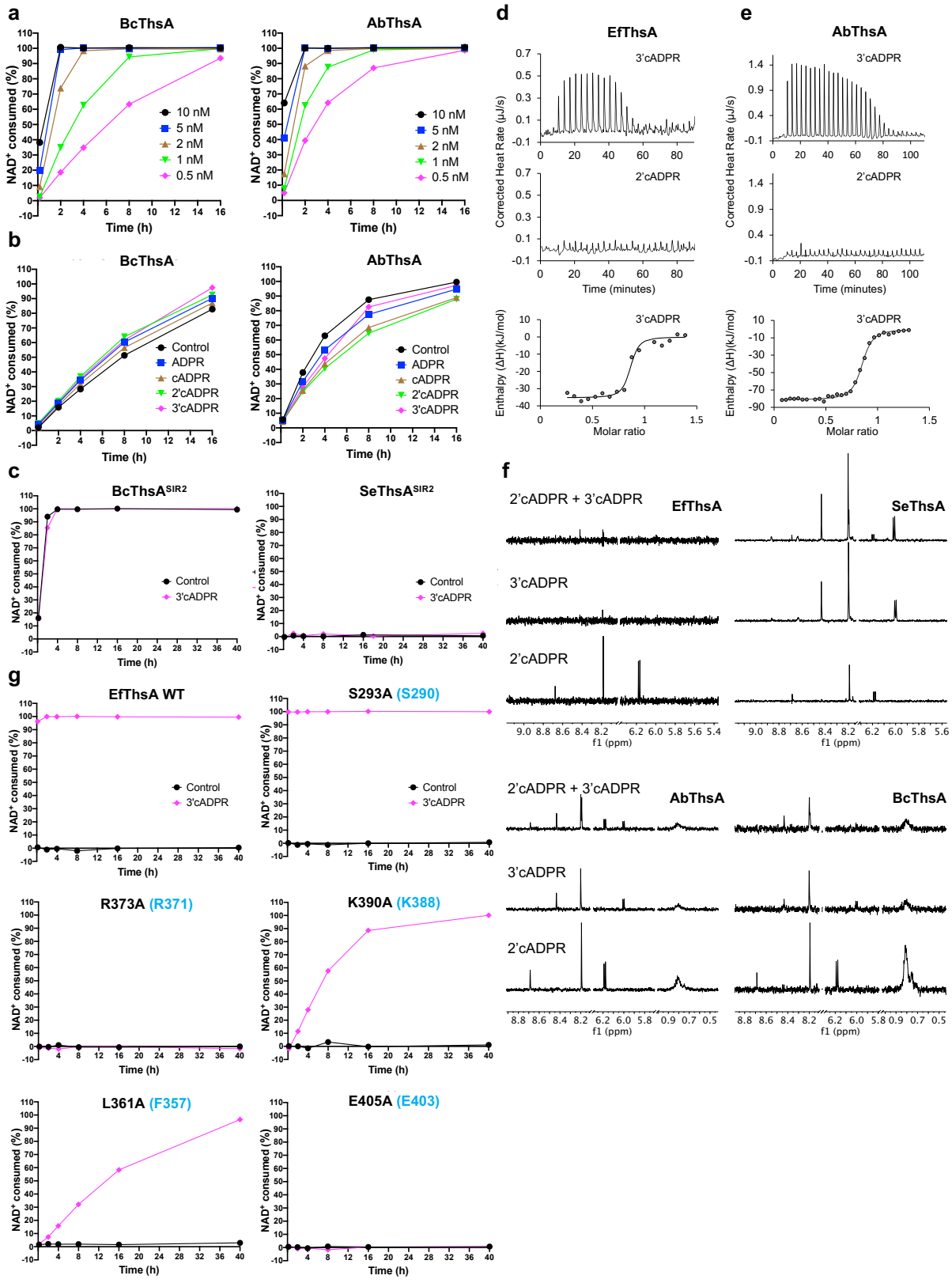
a
BcThsA
AbThsA
NAD+ consumed (%)
Time (h)
10 nM
5 nM
2 nM
1 nM
0.5 nM
b
BcThsA
AbThsA
Control
ADPR
cADPR
2'cADPR
3'cADPR
c
BcThsASIR2
SeThsASIR2
Control
3'cADPR
d
EfThsA
AbThsA
3'cADPR
2'cADPR
Corrected Heat Rate (µJ/s)
Time (minutes)
Enthalpy (ΔH)(kJ/mol)
Molar ratio
e
AbThsA
3'cADPR
2'cADPR
Corrected Heat Rate (µJ/s)
Time (minutes)
Enthalpy (ΔH)(kJ/mol)
Molar ratio
f
2'cADPR + 3'cADPR
EfThsA
SeThsA
3'cADPR
2'cADPR
f1 (ppm)
2'cADPR + 3'cADPR
AbThsA
BcThsA
3'cADPR
2'cADPR
f1 (ppm)
g
EfThsA WT
S293A (S290)
R373A (R371)
K390A (K388)
L361A (F357)
E405A (E403)
NAD+ consumed (%)
Time (h)
Control
3'cADPR

Fig. S10. Characterization of ThsA NADase activity and cADPR isomer interaction by NMR and ITC. (a) NADase activity of BcThsA (0.5 - 10 nM) and AbThsA (0.5 - 10 nM). The initial NAD^+ concentration was 500 μM. (b) Activation of BcThsA (0.5 nM) and AbThsA (0.5 nM) NADase activity by 500 μM ADPR, cADPR, v-cADPR (2'cADPR) and v2-cADPR (3'cADPR). The initial NAD^+ concentration was 500 μM. (c) NADase activity of $BcThsA^{SIR2}$ (0.5 nM) and $SeThsA^{SIR2}$ (10 μM) in the absence and presence of 50 μM v2-cADPR (3'cADPR). Initial NAD^+ concentration was 500 μM. (d) Raw (top panel) and integrated (bottom panel) ITC data for the titration of 0.3 mM v2-cADPR (3'cADPR) with 35 μM EfThsA and raw ITC data for the titration of 0.3 mM v-cADPR (2'cADPR) with 35 μM EfThsA (middle panel). (e) Raw (top panel) and integrated (bottom panel) ITC data for the titration of 0.3 mM v2-cADPR (3'cADPR) with 50 μM AbThsA and raw ITC data for the titration of 0.3 mM v-cADPR (2'cADPR) with 50 μM AbThsA (middle panel). (f) STD NMR competition of v-cADPR (2'cADPR) vs v2-cADPR (3'cADPR) binding to EfThsA, SeThsA, AbThsA and BcThsA The protein concentration was 20 μM and the ligand concentration was 1 mM. (g) Effects of mutations on EfThsA (0.5 μM) NADase activity in the absence and presence of 50 μM v2-cADPR (3'cADPR). Initial NAD^+ concentration was 500 μM. The corresponding residues in BcThsA are shown in blue.

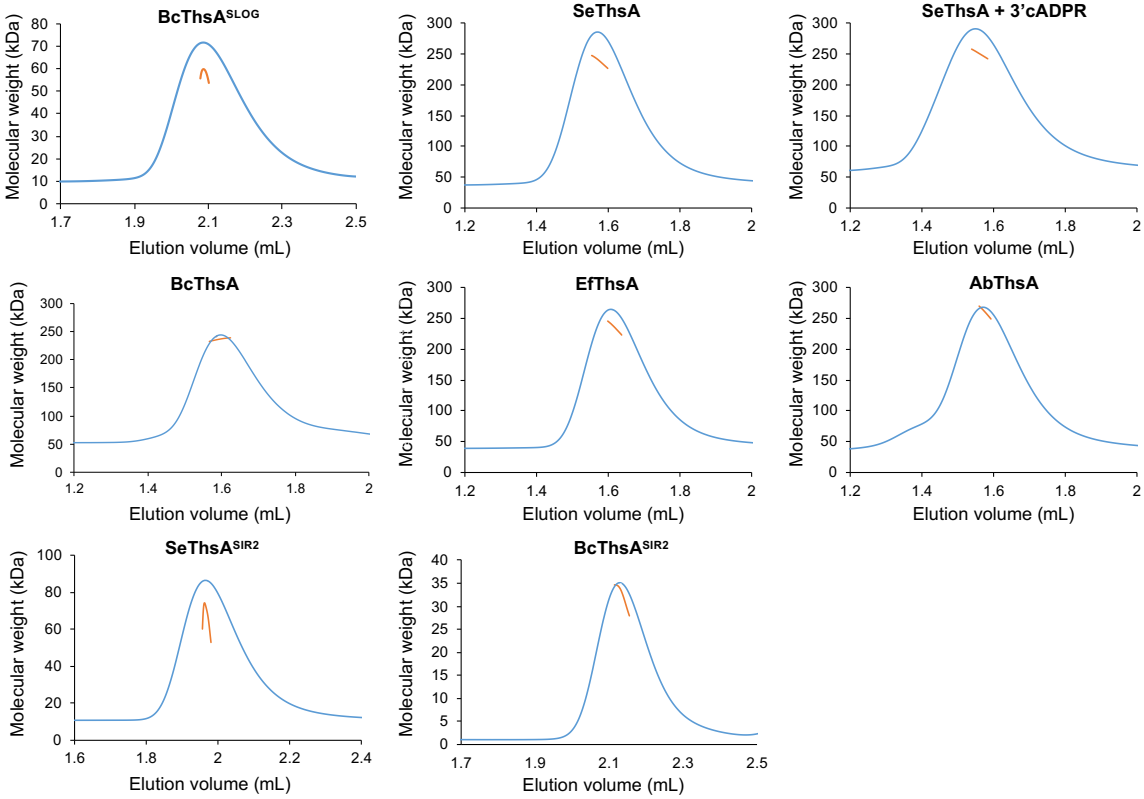
BcThsA^SLOG
SeThsA
SeThsA + 3'cADPR
BcThsA
EfThsA
AbThsA
SeThsA^SIR2
BcThsA^SIR2
Molecular weight (kDa)
Elution volume (mL)

Fig. S11. SEC-MALS analysis of ThsA proteins. The blue line represents the refractive index trace, while the orange line represents the average molecular mass distribution across the peak.

5

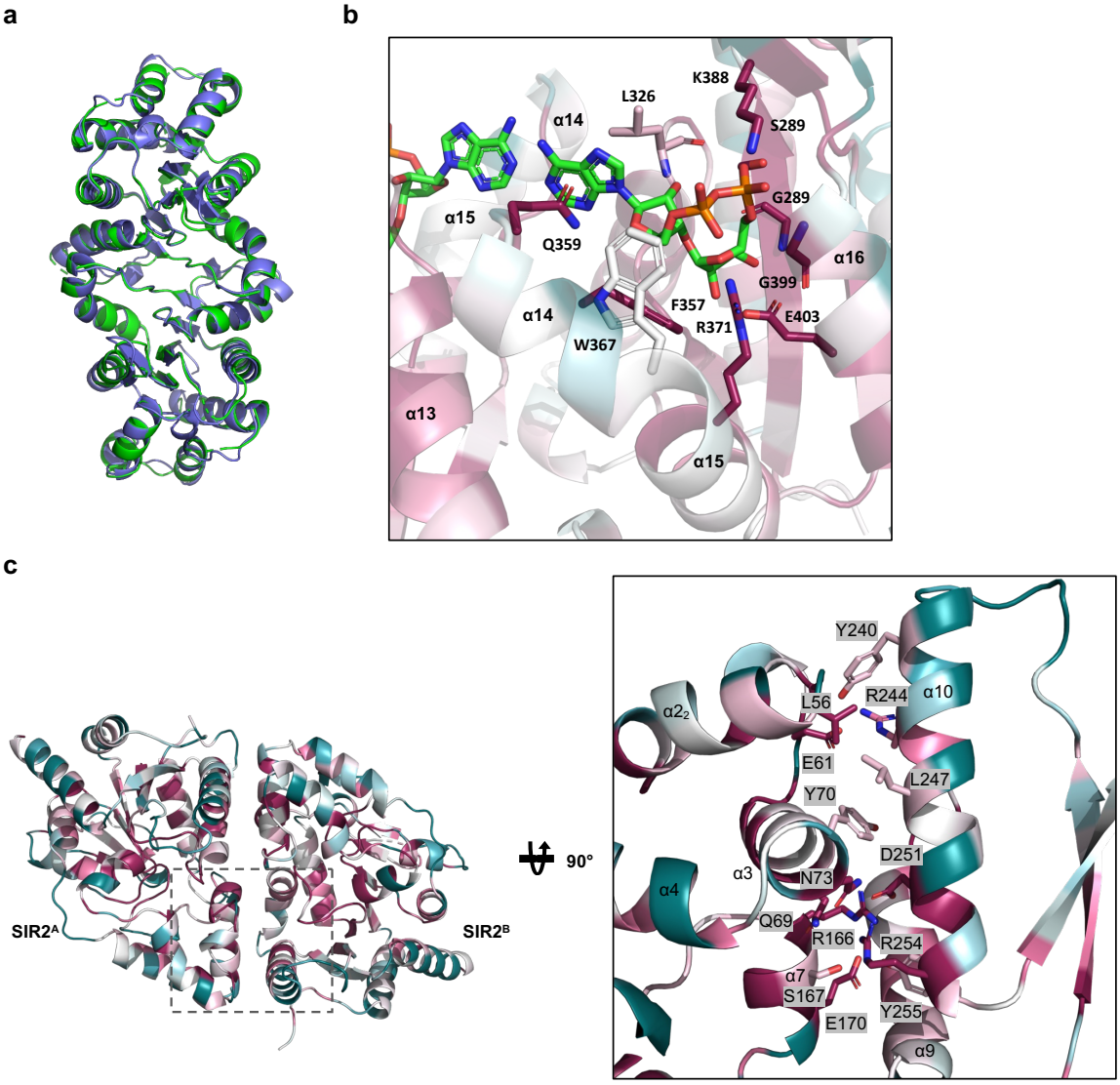
a
b
K388
L326
S289
α14
G289
α15
Q359
α16
G399
F357
α14
E403
R371
W367
α13
α15
c
SIR2A
SIR2B
90°
Y240
α2
L56
R244
α10
E61
L247
Y70
D251
α3
N73
α4
Q69
R166
R254
α7
S167
Y255
E170
α9

Fig. S12. Structural analyses of BcThsA and SeThsA. (a) Structural superposition of $BcThsA^{SLOG}$:v2-cADPR and BcThsA (PDB: 6LHX). The dimeric structures are almost identical (RMSD value of 0.472 Å for 308 Cα atoms). (b) Enlarged cutaway of the v2-cADPR (3'cADPR)-binding pocket in the $BcThsA^{SLOG}$ structure, coloured by sequence conservation. Teal corresponds to variable regions, while purple corresponds to conserved regions. Sequence conservation was calculated by ConSurf (*81*). (c) SeThsA SIR2 dimer coloured by sequence conservation. The insert shows an enlarged cutaway of one half of the symmetric dimer interface, with buried interface residues highlighted in stick representation.

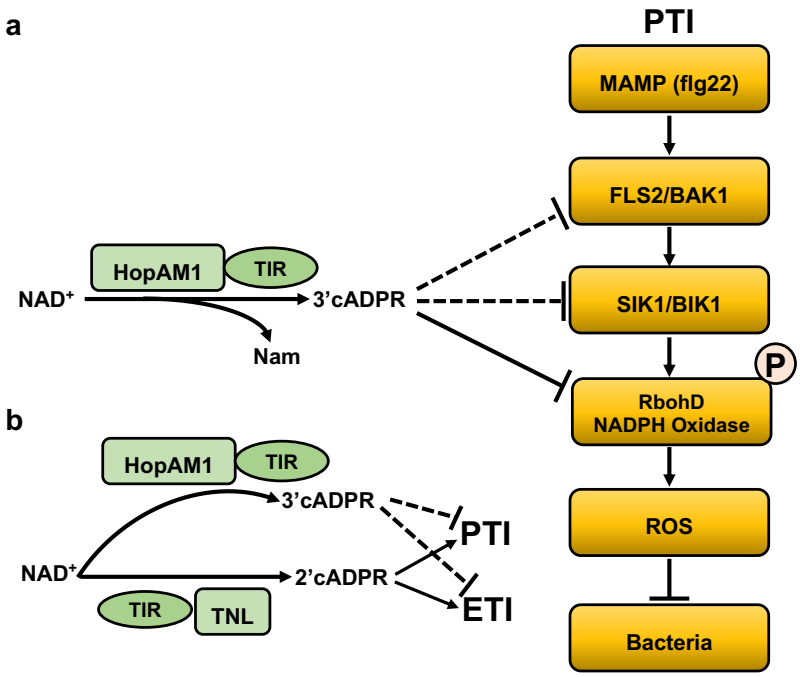
a
PTI
MAMP (flg22)
FLS2/BAK1
HopAM1
TIR
NAD+
3'cADPR
Nam
SIK1/BIK1
P
RbohD
NADPH Oxidase
b
HopAM1
TIR
3'cADPR
PTI
NAD+
2'cADPR
ETI
TIR
TNL
ROS
Bacteria

Fig. S13. Two non-exclusive models for suppression of pattern-triggered immunity by HopAM1. For background, please see (*82-84*). (a) Pattern-triggered immunity (PTI) signaling is triggered by flg22. Upon recognition by the pattern receptor FLS2/BAK1 complex, the MAP4 kinase SIK1 binds and phosphorylates the receptor-like cytoplasmic kinase BIK1 (BOTRYTIS-INDUCED KINASE 1), the central immune regulator, and in turn phosphorylates RbohD NADPH oxidase, leading to a ROS burst that restricts bacterial growth. The HopAM1 TIR-domain NADase produces v2-cADPR (3'cADPR), which interacts with RbohD NADPH oxidase and inhibits its ability to transfer electrons to oxygen and produce superoxide radical O_2^-. (b) Plant TIR-domain signaling mutants exhibit attenuated PTI responses, thus it is also possible that HopAM1 competes with TNLs for NAD^+, producing v2-cADPR (3'cADPR) that either acts as a "dead-end" product and/or antagonizes plant v-cADPR (2'cADPR) signaling downstream of TNLs, such as the EDS signaling complex. MAMP, microbe-associated molecular pattern; ROS, reactive oxygen species.

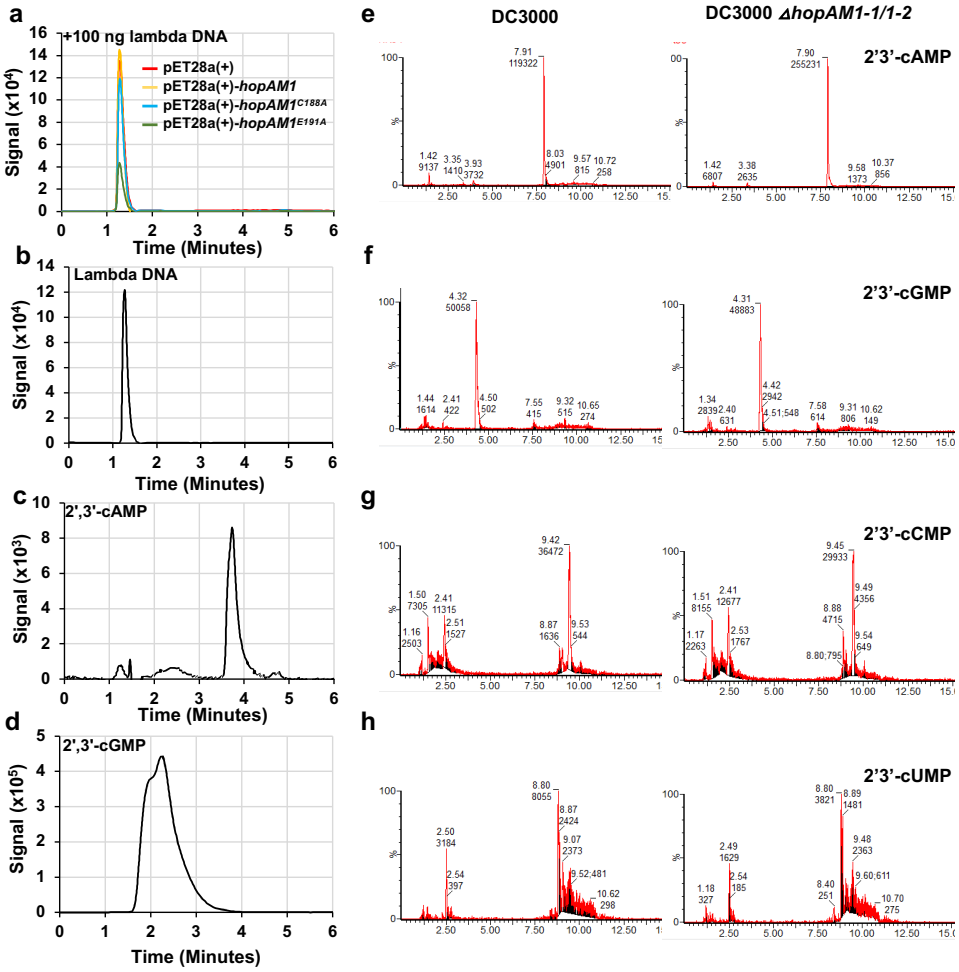
a
+100 ng lambda DNA
pET28a(+)
pET28a(+)-hopAM1
pET28a(+)-hopAM1C188A
pET28a(+)-hopAM1E191A
Signal (x10⁴)
Time (Minutes)
b
Lambda DNA
Signal (x10⁴)
Time (Minutes)
c
2',3'-cAMP
Signal (x10³)
Time (Minutes)
d
2',3'-cGMP
Signal (x10⁵)
Time (Minutes)
e
DC3000
DC3000 ΔhopAM1-1/1-2
2'3'-cAMP
f
2'3'-cGMP
g
2'3'-cCMP
h
2'3'-cUMP

Fig. S14. HopAM1 does not contribute to altered 2',3'-cNMP levels in infected leaves. (a-e) Purified His-tagged HopAM1 protein was incubated with 100 ng lambda DNA overnight, and products detected by HPLC; *in vitro* NADase assays (a); *in vitro* assay with DNA as a substrate (b); lambda DNA (c); 2',3'-cAMP (d); 2',3'-cGMP (e). (f-g) 3'cADPR production but no 2',3'-cGMP accumulation in HopAM1 transgenic Arabidopsis. Expression of HopAM1 was induced with estradiol; 3'cADPR production (f); 2',3'-cGMP standard (g). (h) LC-MS/MS of 2'3'cNMP in *A. thaliana* Col-0 challenged with virulent *Pseudomonas syringae* pv. tomato strain DC3000 or DC3000 lacking both HopAM1-1 and HopAM1-2. Bacterial inoculum was OD_{600}nm 0.15 and leaves were harvested 18 h post-inoculation, snap-frozen, freeze-dried and extracted in 10% methanol, 1% acetic acid. 2',3'-cNMPs were identified by multiple-reaction monitoring, using predicted transitions or in the case of 2'3'cAMP, against a validated standard.

Table S1. List of TIR domain-containing proteins used in this study. "-" means unknown, "?" means the TIR domain has not been shown to produce the products directly.

5

TIR domain-containing proteins analyzed or discussed in this study	Organism	Function	Substrate	ADPR-related products	PDB ID	References
Bacterial TIR domains						
AbTir	*Acinetobacter baumannii 1295743*	-	NAD^+, $NADP^+$	2' cADPR	7UWG	(*15*), this study
BtTir (Btheta7330_RS03065)	*Bacteroides thetaiotaomicron 7330*	-	NAD^+	2' cADPR	7UXR	(*31*), this study
PdTir	*Paracoccus denitrificans* PD1222	Suppression of animal immunity	NAD^+	ADPR?	3H16	(*15, 28*)
TcpB	*Brucella melitensis*	Suppression of animal immunity	NAD^+	2' cADPR	4C7M	(*15, 20, 27, 46*)
BXY_39700	*Bacteroides xylanisolvens* XB1A	-	NAD^+	2' cADPR	-	(*31*), this study
AaTir	*Aquimarina amphilecti*	-	NAD^+, $NADP^+$	3' cADPR	-	(*31*), this study
DORFOR_RS09155	*Dorea formicigenerans* ATCC 27755	-	NAD^+	3' cADPR	-	(*31*), this study
HopAM1	*Pseudomonas syringae* DC3000	Suppression of plant immunity	NAD^+	3' cADPR	-	(*21*), this study
Bovatus_RS22005	*Bacteroides ovatus* ATCC 8483	-	NAD^+	cADPR	-	(*31*), this study
AMN69_RS28245	*Bacteroides thetaiotaomicron* 3731	-	NAD^+	cADPR	-	(*31*), this study
PROVRUST_05034	*Providencia rustigianii DSM 4541*	-	NAD^+	3' cADPR	-	(*31*), this study
AMN69_RS06490	*Bacteroides thetaiotaomicron* 3731	-	NAD^+	cADPR	-	(*31*), this study
CLOBOL_01188	*Clostridium bolteae* ATCC BAA 613	-	NAD^+	ADPR	-	(*31*), this study
Plant TIR domains						
ROQ1	*Nicotiana benthamiana*	Plant immunity	NAD^+	ADPR, 2'cADPR	7JLX	(*35*), this study
L6	*Linum usitatissimum*	Plant immunity	NAD^+, $NADP^+$	ADPR, 2'cADPR	3OZI	(*48*), this study
RUN1	*Vitis rotundifolia*	Plant immunity	NAD^+, $NADP^+$	ADPR	6O0W	(*13*)
RPP1	*Arabidopsis thaliana*	Plant immunity	NAD^+	2' cADPR, pRib-AMP?, pRib-ADP?	7CRC	(*14, 32-34*)

Animal TIR domains						
SARM1	*Homo sapiens*	Executioner of axon degeneration and adaptor protein in animal immunity	NAD^+, $NADP^+$	ADPR, cADPR	6O0R	(*13, 16*)
TIR-STING	*Crassostrea gigas*	-	-	-	6WT7	(*10*)
MyD88	*Homo sapiens*	Toll-like receptor adaptor protein	-	-	7L6W	(*5*)
MAL	*Homo sapiens*	Toll-like receptor adaptor protein	-	-	5UZB	(*7*)

Table S2. Assignments of v-cADPR (2'cADPR) NMR peaks (the structure shown in Fig. 1).

Position #	^{1}H (ppm), splitting, J (Hz)	^{1}H-^{1}H COSY	^{13}C (ppm)	^{1}H-^{13}C HMBC
1				
2	8.36, s		144.7	C6, C4, C5
3				
4			148.8	
5			118.4	
6			150.0	
7				
8	8.85, s		142.6	C5, C4, C6, C1'
9				
1'	6.22, d, 8.7	H2'	84.7	C8, C2', C4
2'	4.90, dd, 8.7/4.7	H1', H3'	75.5	C1", C1', C3', C4'
3'	4.48, d, 4.7	H2'	72.1	C1', C4', C5', C2'
4'	4.41, broad		86.0	C3', C5', C1', C2'
5'	4.15/4.06, m	H5' self	65.3	C4', C3'
1"	5.16, d, 5.0	H2"	105.3	C2', C4", C3", C2"
2"	3.45, t, 5.0	H1", H3"	72.3	C1", C4"
3"	3.99, dd, 5.2/3.6	H2"	70.1	C1", C5"
4"	4.07, m		82.7	C5"
5"	4.07/3.94, m	H5" self	65.7	C4", C3"

Table S3. Assignments of v2-cADPR (3'cADPR) NMR peaks (the structure is shown in Fig. 1).

Position #	^{1}H (ppm), splitting, J (Hz)	^{1}H-^{1}H COSY	^{13}C (ppm)	^{1}H-^{13}C HMBC
1				
2	8.36, s		144.6	C6, C4, C5
3				
4			148.5	
5			118.5	
6			149.9	
7				
8	8.52, s		142.4	C5, C4, C6, C1'
9				
1'	6.06, d, 6.6	H2'	87.2	C8, C4, C2', C3', C4'
2'	4.71, broad	H1', H3'	73.6	C1', C4', C3'
3'	4.94, dd, 3.1/6.1	H2', H4'	69.5	C1', C1", C5', C2'
4'	4.40, m	H3', H5'	84.1	C3', C5'
5'	4.06/4.12, m	H4', H5' self	64.4	C4', C3'
1"	5.34, d, 4.4	H2"	105.7	C3', C3", C2", C4"
2"	4.22, m	H1", H3"	71.8	C1", C4"
3"	4.23, m	H2", H4"	70.6	C4", C5"
4"	4.14, m	H3", H5"	82.8	C3", C5"
5"	4.02/4.14, m	H4", H5" self	66.1	C4", C3", C5" self

Table S4. Assignments of NMR peaks of v2-cADPR (3'cADPR) purified from *N. benthamiana* leaves expressing the bacterial effector HopAM1.

Position #	^{1}H (ppm), splitting, J (Hz)	^{13}C (ppm)	^{1}H-^{13}C HMBC	^{13}C-^{31}P J (Hz)
1				
2	8.15, s	153.0	C4, C6	
3				
4		149.6		
5		118.8		
6		155.7		
7				
8	8.39, s	139.6	C4, C5	
9				
1'	5.98, d, 7.7	85.6	C2', C4, C8	
2'	4.74, broad	72.8	C1'	
3'	4.93, dd, 1.2/5.9	69.4	C1', C1", C5'	
4'	4.36, broad	84.1	C3', C5'	9.4
5'	4.09/3.97, m	64.6	C3', C4'	broad
1"	5.35, d, 4.9	105.8	C3', C4"	
2"	4.23, m	71.7	C1", C4"	
3"	4.22, m	70.7	C1", C5"	
4"	4.14, m	83.0	C3", C5"	9.6
5"	4.01/4.11, m	66.1	C3", C4"	

Table S5. Crystallographic data collection and refinement statistics.

	$AbTir^{TIR}$	$BtTir^{TIR}$	$BcThsA^{SLOG}$: 3'cADPR	SeThsA
PDB ID	7UWG	7UXR	7UXS	7UXT
Data collection				
Space group	P 1 2_1 1	P 1 2_1 1	P 2_1 2_1 2_1	C 2 2 2_1
a, *b*, *c* (Å)	54.68, 67.77, 72.17	37.69, 43.13, 98.76	46.19, 70.80, 121.74	98.81, 274.36, 89.54
α, β, γ (°)	90, 110.46, 90	90, 90.04, 90	90, 90, 90	90, 90, 90
Resolution (Å)	47.86 - 2.16 (2.24 - 2.16)	43.13 - 1.42 (1.44 - 1.42)	46.16 - 1.57 (1.59 - 1.57)	92.96 - 3.40 (3.67 - 3.40)
Total reflections	98,447 (8,184)	40,7463 (17,679)	373,868 (16,957)	104,826 (22,027)
Unique reflections	25,989 (2,180)	59,368 (2,685)	56,724 (2,652)	17,169 (3,473)
Completeness (%)	97.9 (95.3)	98.2 (88.8)	99.7 (95.2)	99.8 (99.9)
Multiplicity	3.8 (3.8)	6.9 (6.6)	6.6 (6.4)	6.1 (6.3)
Wilson B-factor ($Å^2$)	25	16	14	97
R-meas	0.14 (0.77)	0.07 (1.27)	0.04 (0.26)	0.12 (1.42)
R-merge	0.12 (0.66)	0.07 (1.17)	0.04 (0.24)	0.11 (1.31)
R-pim	0.10 (0.52)	0.03 (0.48)	0.02 (0.10)	0.05 (0.56)
Mean I/sigma(I)	7.6 (1.7)	11.2 (0.9)	20.2 (4.6)	6.7 (1.4)
$CC_{1/2}$	0.99 (0.77)	0.99 (0.65)	0.99 (0.97)	0.99 (0.40)
Refinement				
Resolution (Å)	47.86 - 2.16	39.52 - 1.42	36.87 - 1.57	74.98 - 3.40
Reflections used in refinement	25,974	59,326	56,645	17,149
R-work	0.186	0.189	0.149	0.235
R-free	0.229	0.208	0.176	0.291
Number of non-hydrogen atoms	4653	2493	3606	7581
Macromolecules	4372	2328	3154	7559
Ligands	44	0	87	16
Solvent	237	165	365	0
Protein residues	545	285	390	936
RMS bonds (Å)	0.002	0.009	0.008	0.003
RMS angles (°)	0.62	1.05	0.945	0.641
Ramachandran favoured (%)	96.83	96.70	96.63	94.85
Ramachandran allowed (%)	3.17	3.30	3.37	5.04
Ramachandran outliers (%)	0	0	0	0.11
Rotamer outliers (%)	0.8	0	0	0

Clash-score	2.97	3.00	1.00	2.98
Average B-factor (Å ^{2})	30	27	18	146
Macromolecules	29	27	17	146
Ligands	SO_4: 40 PEG: 39	-	3'cADPR: 11 Glycerol: 25 SO_4: 19	PEG:123 Glycerol: 127
Solvent	30	34	29	-

The values in parentheses are for the highest-resolution shell. The statistics were calculated using Aimless (*65*) and MolProbity (*70*). $R_{merge} = \sum_{hkl}\sum_j |I_{hkl,j} - < I_{hkl} > |/(\sum_{hkl}\sum_j I_{hkl,j})$. R_{work} / $R_{free} = \sum_{hkl}\left|F_{hkl}^{obs} - F_{hkl}^{calc}\right|/(\sum_{hkl}F_{hkl}^{obs})$; R_{free} was calculated using randomly chosen 3.5-10 % fraction of data that was excluded from refinement.

Table S6. Cryo-EM analysis of AbTir^{TIR}:3AD.

Data collection and processing	
Cryo-EM facility	University of Queensland
Microscope	JEOL CryoARM 300
Detector	Gatan K3
Voltage (kV)	300
Nominal magnification	60,000
Pixel size (Å)	0.80
Defocus range (μm)	-0.5 to -3.0
Total exposure (e/Å^2)	40
Exposure per frame (e/Å^2)	0.80
Total micrographs (no.)	2,019
Total extracted particles (no.)	730,607
Final particles (no.)	272,949
Symmetry imposed	C1
Map sharpening B-factor (Å^2)	127.6
Resolution (FSC) (Å)	
Masked (0.143)	2.9
Unmasked (0.143)	2.9
Model composition	
Number of chains	4
Atoms	8,896 (hydrogens: 4,388)
Residues	536
Water	0
Ligands	**3AD**: 4 molecules
Model validation	
Bonds (RMSD)	
Lengths (Å) (> 4σ)	0.005 (0)
Angles (°) (> 4σ)	0.892 (0)
MolProbity score	0.5
Clash-score	0
Ramachandran plot (%)	

Outliers	0
Allowed	1.89
Favored	98.11
Rotamer outliers (%)	0
Cβ≤ outliers (%)	0
Peptide plane (%)	
Cis proline/general	0.0/0.0
Twisted proline/general	0.0/0.0
CaBLAM outliers (%)	0.77
ADP B-factor (min/max/mean; Å^2)	
Protein	12.24/58.70/33.51
Ligand	18.47/46.32/32.90
Occupancy = 1 (%)	100
Map to model FSC (0.143/0.5, Å)	2.6/2.7/2.8
Map correlation coefficient	
Volume	0.83
Ligand (mean)	0.81

The statistics were calculated using CryoSPARC (*74*) and the phenix.validation_cryoem tool (*85*).

5

Table S7. Estimated changes of NAD^+, ADPR, and 2'cADPR amounts based on ^1H NMR assays of $AbTir^{TIR}$ mutants. Protein concentration was 50 μM and initial NAD^+ concentration was 500 μM unless otherwise noted

AbTir^{TIR}		% change at 10 min			% change at 24 h		
		NAD^+	ADPR	2'cADPR	NAD^+	ADPR	2'cADPR
	WT	-100	0	+100	-100	+1	+99
BB loop	G174A	0	0	0	0	0	0
	D175A	-100	+3	+97	-100	+3	+97
	S176A	-2	0	+2	-8	0	+8
	L177A	-89	+13	+76	-99	+15	+84
αB	R178A[1]	-1	0	+1	-5	+1	+4
	D182A	-4	0	+4	-100	+4	+96
αC	W204A	-10	+6	+4	-100	+71	+29
	T205A	-16	+0	+16	-100	+1	+99
	Y207A	0	0	0	0	0	0
	E208A[2]	0	0	0	-8[3]	+8[3]	0[3]
	E208D[2]	0	0	0	-30[3]	0[3]	+30[3]
	R215A	0	0	0	0	0	0
	E216A	-100	+5	+95	-100	+5	+95

[1] 30 μM protein
[2] 20 μM protein and 1 mM NAD^+
[3] % change at 16 h

Table S8. MALS analysis of ThsA proteins.

	MW (kDa) Monomer[1]	MW (kDa) Dimer[1]	MW (kDa) Tetramer[1]	MW (kDa) MALS	[Protein] (μM)[2]
BcThsA	57.9	115.7	231.5	236.1 +/- 0.5	30.0
SeThsA	57.0	114.1	228.2	237.9 +/- 18.3	17.5
SeThsA + 3'cADPR	57.0	114.1	228.2	250.6 +/- 2.5	17.5
EfThsA	57.7	115.5	231.0	235.5 +/- 3.5	17.3
AbThsA	58.1	116.2	232.3	260.3 +/- 2.6	17.2
$SeThsA^{SIR2}$	33.4	66.7	133.4	60.0 +/- 6.2	30.0
$BcThsA^{SIR2}$	33.2	66.5	132.9	32.3 +/- 1.1	30.1
$BcThsA^{SLOG}$	24.8	49.6	99.2	51.6 +/- 4.1	80.7

[1]Calculated from amino-acid sequence.
[2]Concentration of protein sample loaded onto SEC column.

Table S9. 3'cADPR-interacting residues in BcThsA, EfTshA, SeThsA and AbThsA, based on the BcThsA^{SLOG} crystal structure.

BcThsA	EfThsA	SeThsA	AbThsA	Interacting moiety of 3'cADPR
G289	G292	G288	G287	Distal ribose
S290	S293	S289	S288	Pyrophosphate
L326	L330	K325	L324	Adenine and adenine-linked ribose
F357	L361	F355	F355	Adenine-linked ribose
Q359	L363	Q357	Q357	Adenine and adenine-linked ribose
W367	W369	Y369	W369	Adenine-linked ribose
R371	R373	R373	R373	Pyrophosphate and distal ribose
K388	K390	K390	K390	Pyrophosphate
G399	G401	G398	G407	Pyrophosphate
E403	E405	E402	E411	Distal ribose

References and Notes

1. T. Ve, S. J. Williams, B. Kobe, Structure and function of Toll/interleukin-1 receptor/resistance protein (TIR) domains. *Apoptosis* **20**, 250–261 (2015). doi:10.1007/s10495-014-1064-2 Medline

2. S. Nimma, T. Ve, S. J. Williams, B. Kobe, Towards the structure of the TIR-domain signalosome. *Curr. Opin. Struct. Biol.* **43**, 122–130 (2017). doi:10.1016/j.sbi.2016.12.014 Medline

3. S. Nimma, W. Gu, N. Maruta, Y. Li, M. Pan, F. K. Saikot, B. Y. J. Lim, H. Y. McGuinness, Z. F. Zaoti, S. Li, S. Desa, M. K. Manik, J. D. Nanson, B. Kobe, Structural evolution of TIR-domain signalosomes. *Front. Immunol.* **12**, 784484 (2021). doi:10.3389/fimmu.2021.784484 Medline

4. N. Maruta, H. Burdett, B. Y. J. Lim, X. Hu, S. Desa, M. K. Manik, B. Kobe, Structural basis of NLR activation and innate immune signalling in plants. *Immunogenetics* **74**, 5–26 (2022). doi:10.1007/s00251-021-01242-5 Medline

5. M. T. B. Clabbers, S. Holmes, T. W. Muusse, P. R. Vajjhala, S. J. Thygesen, A. K. Malde, D. J. B. Hunter, T. I. Croll, L. Flueckiger, J. D. Nanson, M. H. Rahaman, A. Aquila, M. S. Hunter, M. Liang, C. H. Yoon, J. Zhao, N. A. Zatsepin, B. Abbey, E. Sierecki, Y. Gambin, K. J. Stacey, C. Darmanin, B. Kobe, H. Xu, T. Ve, MyD88 TIR domain higher-order assembly interactions revealed by microcrystal electron diffraction and serial femtosecond crystallography. *Nat. Commun.* **12**, 2578 (2021). doi:10.1038/s41467-021-22590-6 Medline

6. P. R. Vajjhala, T. Ve, A. Bentham, K. J. Stacey, B. Kobe, The molecular mechanisms of signaling by cooperative assembly formation in innate immunity pathways. *Mol. Immunol.* **86**, 23–37 (2017). doi:10.1016/j.molimm.2017.02.012 Medline

7. T. Ve, P. R. Vajjhala, A. Hedger, T. Croll, F. DiMaio, S. Horsefield, X. Yu, P. Lavrencic, Z. Hassan, G. P. Morgan, A. Mansell, M. Mobli, A. O'Carroll, B. Chauvin, Y. Gambin, E. Sierecki, M. J. Landsberg, K. J. Stacey, E. H. Egelman, B. Kobe, Structural basis of TIR-domain-assembly formation in MAL- and MyD88-dependent TLR4 signaling. *Nat. Struct. Mol. Biol.* **24**, 743–751 (2017). doi:10.1038/nsmb.3444 Medline

8. R. R. Rana, M. Zhang, A. M. Spear, H. S. Atkins, B. Byrne, Bacterial TIR-containing proteins and host innate immune system evasion. *Med. Microbiol. Immunol. (Berl.)* **202**, 1–10 (2013). doi:10.1007/s00430-012-0253-2 Medline

9. S. Doron, S. Melamed, G. Ofir, A. Leavitt, A. Lopatina, M. Keren, G. Amitai, R. Sorek, Systematic discovery of antiphage defense systems in the microbial pangenome. *Science* **359**, eaar4120 (2018). doi:10.1126/science.aar4120 Medline

10. B. R. Morehouse, A. A. Govande, A. Millman, A. F. A. Keszei, B. Lowey, G. Ofir, S. Shao, R. Sorek, P. J. Kranzusch, STING cyclic dinucleotide sensing originated in bacteria. *Nature* **586**, 429–433 (2020). doi:10.1038/s41586-020-2719-5 Medline

11. N. Tal, B. R. Morehouse, A. Millman, A. Stokar-Avihail, C. Avraham, T. Fedorenko, E. Yirmiya, E. Herbst, A. Brandis, T. Mehlman, Y. Oppenheimer-Shaanan, A. F. A. Keszei, S. Shao, G. Amitai, P. J. Kranzusch, R. Sorek, Cyclic CMP and cyclic UMP mediate

bacterial immunity against phages. *Cell* **184**, 5728–5739.e16 (2021). doi:10.1016/j.cell.2021.09.031 Medline

12. B. Koopal, A. Potocnik, S. K. Mutte, C. Aparicio-Maldonado, S. Lindhoud, J. J. M. Vervoort, S. J. J. Brouns, D. C. Swarts, Short prokaryotic Argonaute systems trigger cell death upon detection of invading DNA. *Cell* **185**, 1471–1486.e19 (2022). doi:10.1016/j.cell.2022.03.012 Medline

13. S. Horsefield, H. Burdett, X. Zhang, M. K. Manik, Y. Shi, J. Chen, T. Qi, J. Gilley, J. S. Lai, M. X. Rank, L. W. Casey, W. Gu, D. J. Ericsson, G. Foley, R. O. Hughes, T. Bosanac, M. von Itzstein, J. P. Rathjen, J. D. Nanson, M. Boden, I. B. Dry, S. J. Williams, B. J. Staskawicz, M. P. Coleman, T. Ve, P. N. Dodds, B. Kobe, NAD^+ cleavage activity by animal and plant TIR domains in cell death pathways. *Science* **365**, 793–799 (2019). doi:10.1126/science.aax1911 Medline

14. L. Wan, K. Essuman, R. G. Anderson, Y. Sasaki, F. Monteiro, E. H. Chung, E. Osborne Nishimura, A. DiAntonio, J. Milbrandt, J. L. Dangl, M. T. Nishimura, TIR domains of plant immune receptors are NAD^+-cleaving enzymes that promote cell death. *Science* **365**, 799–803 (2019). doi:10.1126/science.aax1771 Medline

15. K. Essuman, D. W. Summers, Y. Sasaki, X. Mao, A. K. Y. Yim, A. DiAntonio, J. Milbrandt, TIR domain proteins are an ancient family of NAD^+-consuming enzymes. *Curr. Biol.* **28**, 421–430.e4 (2018). doi:10.1016/j.cub.2017.12.024 Medline

16. K. Essuman, D. W. Summers, Y. Sasaki, X. Mao, A. DiAntonio, J. Milbrandt, The SARM1 Toll/interleukin-1 receptor domain possesses intrinsic NAD^+ cleavage activity that promotes pathological axonal degeneration. *Neuron* **93**, 1334–1343.e5 (2017). doi:10.1016/j.neuron.2017.02.022 Medline

17. M. D. Figley, W. Gu, J. D. Nanson, Y. Shi, Y. Sasaki, K. Cunnea, A. K. Malde, X. Jia, Z. Luo, F. K. Saikot, T. Mosaiab, V. Masic, S. Holt, L. Hartley-Tassell, H. Y. McGuinness, M. K. Manik, T. Bosanac, M. J. Landsberg, P. S. Kerry, M. Mobli, R. O. Hughes, J. Milbrandt, B. Kobe, A. DiAntonio, T. Ve, SARM1 is a metabolic sensor activated by an increased NMN/NAD^+ ratio to trigger axon degeneration. *Neuron* **109**, 1118–1136.e11 (2021). doi:10.1016/j.neuron.2021.02.009 Medline

18. H. C. Lee, R. Aarhus, D. Levitt, The crystal structure of cyclic ADP-ribose. *Nat. Struct. Biol.* **1**, 143–144 (1994). doi:10.1038/nsb0394-143 Medline

19. Z. Duxbury, S. Wang, C. I. MacKenzie, J. L. Tenthorey, X. Zhang, S. U. Huh, L. Hu, L. Hill, P. M. Ngou, P. Ding, J. Chen, Y. Ma, H. Guo, B. Castel, P. N. Moschou, M. Bernoux, P. N. Dodds, R. E. Vance, J. D. G. Jones, Induced proximity of a TIR signaling domain on a plant-mammalian NLR chimera activates defense in plants. *Proc. Natl. Acad. Sci. U.S.A.* **117**, 18832–18839 (2020). doi:10.1073/pnas.2001185117 Medline

20. J. M. Coronas-Serna, A. Louche, M. Rodríguez-Escudero, M. Roussin, P. R. C. Imbert, I. Rodríguez-Escudero, L. Terradot, M. Molina, J. P. Gorvel, V. J. Cid, S. P. Salcedo, The TIR-domain containing effectors BtpA and BtpB from *Brucella abortus* impact NAD metabolism. *PLOS Pathog.* **16**, e1007979 (2020). doi:10.1371/journal.ppat.1007979 Medline

21. S. Eastman, T. Smith, M. A. Zaydman, P. Kim, S. Martinez, N. Damaraju, A. DiAntonio, J. Milbrandt, T. E. Clemente, J. R. Alfano, M. Guo, A phytobacterial TIR domain effector

manipulates NAD^+ to promote virulence. *New Phytol.* **233**, 890–904 (2022). doi:10.1111/nph.17805 Medline

22. G. Ofir, E. Herbst, M. Baroz, D. Cohen, A. Millman, S. Doron, N. Tal, D. B. A. Malheiro, S. Malitsky, G. Amitai, R. Sorek, Antiviral activity of bacterial TIR domains via immune signalling molecules. *Nature* **600**, 116–120 (2021). doi:10.1038/s41586-021-04098-7 Medline

23. D. Ka, H. Oh, E. Park, J. H. Kim, E. Bae, Structural and functional evidence of bacterial antiphage protection by Thoeris defense system via NAD^+ degradation. *Nat. Commun.* **11**, 2816 (2020). doi:10.1038/s41467-020-16703-w Medline

24. A. M. Burroughs, L. Aravind, Identification of uncharacterized components of prokaryotic immune systems and their diverse eukaryotic reformulations. *J. Bacteriol.* **202**, e00365–e00320 (2020). doi:10.1128/JB.00365-20 Medline

25. Y. Shi, P. S. Kerry, J. D. Nanson, T. Bosanac, Y. Sasaki, R. Krauss, F. K. Saikot, S. E. Adams, T. Mosaiab, V. Masic, X. Mao, F. Rose, E. Vasquez, M. Furrer, K. Cunnea, A. Brearley, W. Gu, Z. Luo, L. Brillault, M. J. Landsberg, A. DiAntonio, B. Kobe, J. Milbrandt, R. O. Hughes, T. Ve, Structural basis of SARM1 activation, substrate recognition, and inhibition by small molecules. *Mol. Cell* **82**, 1643–1659.e10 (2022). doi:10.1016/j.molcel.2022.03.007 Medline

26. D. Yu, W. Song, E. Y. J. Tan, L. Liu, Y. Cao, J. Jirschitzka, E. Li, E. Logemann, C. Xu, S. Huang, A. Jia, X. Chang, Z. Han, B. Wu, P. Schulze-Lefert, J. Chai, TIR domains of plant immune receptors are 2′,3′-cAMP/cGMP synthetases mediating cell death. *Cell* **185**, 2370–2386.e18 (2022). doi:10.1016/j.cell.2022.04.032 Medline

27. M. Alaidarous, T. Ve, L. W. Casey, E. Valkov, D. J. Ericsson, M. O. Ullah, M. A. Schembri, A. Mansell, M. J. Sweet, B. Kobe, Mechanism of bacterial interference with TLR4 signaling by *Brucella* Toll/interleukin-1 receptor domain-containing protein TcpB. *J. Biol. Chem.* **289**, 654–668 (2014). doi:10.1074/jbc.M113.523274 Medline

28. S. L. Chan, L. Y. Low, S. Hsu, S. Li, T. Liu, E. Santelli, G. Le Negrate, J. C. Reed, V. L. Woods Jr., J. Pascual, Molecular mimicry in innate immunity: Crystal structure of a bacterial TIR domain. *J. Biol. Chem.* **284**, 21386–21392 (2009). doi:10.1074/jbc.C109.007591 Medline

29. B. Kaplan-Türköz, T. Koelblen, C. Felix, M. P. Candusso, D. O'Callaghan, A. C. Vergunst, L. Terradot, Structure of the Toll/interleukin 1 receptor (TIR) domain of the immunosuppressive *Brucella* effector BtpA/Btp1/TcpB. *FEBS Lett.* **587**, 3412–3416 (2013). doi:10.1016/j.febslet.2013.09.007 Medline

30. G. A. Snyder, D. Deredge, A. Waldhuber, T. Fresquez, D. Z. Wilkins, P. T. Smith, S. Durr, C. Cirl, J. Jiang, W. Jennings, T. Luchetti, N. Snyder, E. J. Sundberg, P. Wintrode, T. Miethke, T. S. Xiao, Crystal structures of the Toll/Interleukin-1 receptor (TIR) domains from the *Brucella* protein TcpB and host adaptor TIRAP reveal mechanisms of molecular mimicry. *J. Biol. Chem.* **289**, 669–679 (2014). doi:10.1074/jbc.M113.523407 Medline

31. J. S. Weagley, M. Zaydman, S. Venkatesh, Y. Sasaki, N. Damaraju, A. Yenkin, W. Buchser, D. A. Rodionov, A. Osterman, T. Ahmed, M. J. Barratt, A. DiAntonio, J. Milbrandt, J. I. Gordon, Products of gut microbial Toll/interleukin-1 receptor domain NADase activities

in gnotobiotic mice and Bangladeshi children with malnutrition. *Cell Rep.* **39**, 110738 (2022). doi:10.1016/j.celrep.2022.110738 Medline

32. A. Jia, S. Huang, W. Song, J. Wang, Y. Meng, Y. Sun, L. Xu, H. Laessle, J. Jirschitzka, J. Hou, T. Zhang, W. Yu, G. Hessler, E. Li, S. Ma, D. Yu, J. Gebauer, U. Baumann, X. Liu, Z. Han, J. Chang, J. E. Parker, J. Chai, TIR-catalyzed ADP-ribosylation reactions produce signaling molecules for plant immunity. *Science* **377**, eabq8180 (2022). doi:10.1126/science.abq8180 Medline

33. S. Huang, A. Jia, W. Song, G. Hessler, Y. Meng, Y. Sun, L. Xu, H. Laessle, J. Jirschitzka, S. Ma, Y. Xiao, D. Yu, J. Hou, R. Liu, H. Sun, X. Liu, Z. Han, J. Chang, J. E. Parker, J. Chai, Identification and receptor mechanism of TIR-catalyzed small molecules in plant immunity. *Science* **377**, eabq3297 (2022). doi:10.1126/science.abq3297 Medline

34. S. Ma, D. Lapin, L. Liu, Y. Sun, W. Song, X. Zhang, E. Logemann, D. Yu, J. Wang, J. Jirschitzka, Z. Han, P. Schulze-Lefert, J. E. Parker, J. Chai, Direct pathogen-induced assembly of an NLR immune receptor complex to form a holoenzyme. *Science* **370**, eabe3069 (2020). doi:10.1126/science.abe3069 Medline

35. R. Martin, T. Qi, H. Zhang, F. Liu, M. King, C. Toth, E. Nogales, B. J. Staskawicz, Structure of the activated ROQ1 resistosome directly recognizing the pathogen effector XopQ. *Science* **370**, eabd9993 (2020). doi:10.1126/science.abd9993 Medline

36. M. de Torres Zabala, G. Littlejohn, S. Jayaraman, D. Studholme, T. Bailey, T. Lawson, M. Tillich, D. Licht, B. Bölter, L. Delfino, W. Truman, J. Mansfield, N. Smirnoff, M. Grant, Chloroplasts play a central role in plant defence and are targeted by pathogen effectors. *Nat. Plants* **1**, 15074 (2015). doi:10.1038/nplants.2015.74 Medline

37. S. Breen, R. Hussain, E. Breeze, H. Brown, I. Alzwiy, S. Abdelsayed, T. Gaikwad, M. Grant, Chloroplasts play a central role in facilitating MAMP-triggered immunity, pathogen suppression of immunity and crosstalk with abiotic stress. *Plant Cell Environ.* pce.14408 (2022). doi:10.1111/pce.14408 Medline

38. M. T. Hulin, W. Ma, Pangenomics facilitated with structural analysis reveals host NAD^+ manipulation as a major virulence activity of bacterial effectors. bioRxiv 2022.2006.2007.495176 [Preprint] (2022); https://doi.org/10.1101/2022.06.07.495176.

39. S. Eastman, A. Bayless, M. Guo, The nucleotide revolution: Immunity at the intersection of TIR-domains, nucleotides, and Ca^2. *Mol. Plant Microbe Interact.* MPMI-06-22-0132-CR (2022). doi:10.1094/MPMI-06-22-0132-CR Medline

40. K. Essuman, J. Milbrandt, J. L. Dangl, M. T. Nishimura, Shared TIR enzymatic functions regulate cell death and immunity across the tree of life. *Science* **377**, eabo0001 (2022). doi:10.1126/science.abo0001 Medline

41. M. Howard, J. C. Grimaldi, J. F. Bazan, F. E. Lund, L. Santos-Argumedo, R. M. Parkhouse, T. F. Walseth, H. C. Lee, Formation and hydrolysis of cyclic ADP-ribose catalyzed by lymphocyte antigen CD38. *Science* **262**, 1056–1059 (1993). doi:10.1126/science.8235624 Medline

42. L. Aravind, D. Zhang, R. F. de Souza, S. Anand, L. M. Iyer, The natural history of ADP-ribosyltransferases and the ADP-ribosylation system. *Curr. Top. Microbiol. Immunol.* **384**, 3–32 (2015). doi:10.1007/82_2014_414 Medline

43. K. Ueda, O. Hayaishi, ADP-ribosylation. *Annu. Rev. Biochem.* **54**, 73–100 (1985). doi:10.1146/annurev.bi.54.070185.000445 Medline

44. G. Hogrel, A. Guild, S. Graham, H. Rickman, S. Grüschow, Q. Bertrand, L. Spagnolo, M. F. White, Cyclic nucleotide-induced helical structure activates a TIR immune effector. *Nature* **608**, 808–812 (2022). doi:10.1038/s41586-022-05070-9 Medline

45. B. R. Morehouse, M. C. J. Yip, A. F. A. Keszei, N. K. McNamara-Bordewick, S. Shao, P. J. Kranzusch, Cryo-EM structure of an active bacterial TIR-STING filament complex. *Nature* **608**, 803–807 (2022). doi:10.1038/s41586-022-04999-1 Medline

46. A. Chaudhary, K. Ganguly, S. Cabantous, G. S. Waldo, S. N. Micheva-Viteva, K. Nag, W. S. Hlavacek, C. S. Tung, The *Brucella* TIR-like protein TcpB interacts with the death domain of MyD88. *Biochem. Biophys. Res. Commun.* **417**, 299–304 (2012). doi:10.1016/j.bbrc.2011.11.104 Medline

47. C. Felix, B. Kaplan Türköz, S. Ranaldi, T. Koelblen, L. Terradot, D. O'Callaghan, A. C. Vergunst, The *Brucella* TIR domain containing proteins BtpA and BtpB have a structural WxxxE motif important for protection against microtubule depolymerisation. *Cell Commun. Signal.* **12**, 53 (2014). doi:10.1186/s12964-014-0053-y Medline

48. M. Bernoux, T. Ve, S. Williams, C. Warren, D. Hatters, E. Valkov, X. Zhang, J. G. Ellis, B. Kobe, P. N. Dodds, Structural and functional analysis of a plant resistance protein TIR domain reveals interfaces for self-association, signaling, and autoregulation. *Cell Host Microbe* **9**, 200–211 (2011). doi:10.1016/j.chom.2011.02.009 Medline

49. Q. Liu, R. Graeff, I. A. Kriksunov, H. Jiang, B. Zhang, N. Oppenheimer, H. Lin, B. V. Potter, H. C. Lee, Q. Hao, Structural basis for enzymatic evolution from a dedicated ADP-ribosyl cyclase to a multifunctional NAD hydrolase. *J. Biol. Chem.* **284**, 27637–27645 (2009). doi:10.1074/jbc.M109.031005 Medline

50. R. Graeff, Q. Liu, I. A. Kriksunov, M. Kotaka, N. Oppenheimer, Q. Hao, H. C. Lee, Mechanism of cyclizing NAD to cyclic ADP-ribose by ADP-ribosyl cyclase and CD38. *J. Biol. Chem.* **284**, 27629–27636 (2009). doi:10.1074/jbc.M109.030965 Medline

51. A. Leavitt, E. Yirmiya, G. Amitai, A. Lu, J. Garb, B. R. Morehouse, S. J. Hobbs, P. J. Kranzusch, R. Sorek, Viruses inhibit TIR gcADPR signaling to overcome bacterial defense. bioRxiv 2022.2005.2003.490397 [Preprint] (2022); https://doi.org/10.1101/2022.05.03.490397.

52. A. M. Burroughs, D. Zhang, D. E. Schäffer, L. M. Iyer, L. Aravind, Comparative genomic analyses reveal a vast, novel network of nucleotide-centric systems in biological conflicts, immunity and signaling. *Nucleic Acids Res.* **43**, 10633–10654 (2015). doi:10.1093/nar/gkv1267 Medline

53. T. Kuroha, H. Tokunaga, M. Kojima, N. Ueda, T. Ishida, S. Nagawa, H. Fukuda, K. Sugimoto, H. Sakakibara, Functional analyses of *LONELY GUY* cytokinin-activating enzymes reveal the importance of the direct activation pathway in *Arabidopsis*. *Plant Cell* **21**, 3152–3169 (2009). doi:10.1105/tpc.109.068676 Medline

54. M. S. Drenichev, M. Bennett, R. A. Novikov, J. Mansfield, N. Smirnoff, M. Grant, S. N. Mikhailov, A role for 3′-O-β-D-ribofuranosyladenosine in altering plant immunity. *Phytochemistry* **157**, 128–134 (2019). doi:10.1016/j.phytochem.2018.10.016 Medline

55. M. Z. Li, S. J. Elledge, Harnessing homologous recombination in vitro to generate recombinant DNA via SLIC. *Nat. Methods* **4**, 251–256 (2007). doi:10.1038/nmeth1010 Medline

56. W. T. Mooij, E. Mitsiki, A. Perrakis, ProteinCCD: Enabling the design of protein truncation constructs for expression and crystallization experiments. *Nucleic Acids Res.* **37**, W402–W405 (2009). doi:10.1093/nar/gkp256 Medline

57. L. Stols, M. Gu, L. Dieckman, R. Raffen, F. R. Collart, M. I. Donnelly, A new vector for high-throughput, ligation-independent cloning encoding a tobacco etch virus protease cleavage site. *Protein Expr. Purif.* **25**, 8–15 (2002). doi:10.1006/prep.2001.1603 Medline

58. F. W. Studier, Protein production by auto-induction in high density shaking cultures. *Protein Expr. Purif.* **41**, 207–234 (2005). doi:10.1016/j.pep.2005.01.016 Medline

59. G. Pergolizzi, J. N. Butt, R. P. Bowater, G. K. Wagner, A novel fluorescent probe for NAD-consuming enzymes. *Chem. Commun.* **47**, 12655–12657 (2011). doi:10.1039/c1cc15499k Medline

60. M. Piotto, V. Saudek, V. Sklenár, Gradient-tailored excitation for single-quantum NMR spectroscopy of aqueous solutions. *J. Biomol. NMR* **2**, 661–665 (1992). doi:10.1007/BF02192855 Medline

61. V. Sklenar, M. Piotto, R. Leppik, V. Saudek, Gradient-tailored water suppression for ^{1}H-^{15}N HSQC experiments optimized to retain full sensitivity. *J. Magn. Reson. A* **102**, 241–245 (1993). doi:10.1006/jmra.1993.1098

62. M. Mayer, B. Meyer, Characterization of ligand binding by saturation transfer difference NMR spectroscopy. *Angew. Chem. Int. Ed.* **38**, 1784–1788 (1999). doi:10.1002/(SICI)1521-3773(19990614)38:12<1784:AID-ANIE1784>3.0.CO;2-Q Medline

63. A. Chaikuad, S. Knapp, F. von Delft, Defined PEG smears as an alternative approach to enhance the search for crystallization conditions and crystal-quality improvement in reduced screens. *Acta Crystallogr. D Biol. Crystallogr.* **71**, 1627–1639 (2015). doi:10.1107/S1399004715007968 Medline

64. W. Kabsch, XDS. *Acta Crystallogr. D Biol. Crystallogr.* **66**, 125–132 (2010). doi:10.1107/S0907444909047337 Medline

65. P. Evans, Scaling and assessment of data quality. *Acta Crystallogr. D Biol. Crystallogr.* **62**, 72–82 (2006). doi:10.1107/S0907444905036693 Medline

66. P. D. Adams, D. Baker, A. T. Brunger, R. Das, F. DiMaio, R. J. Read, D. C. Richardson, J. S. Richardson, T. C. Terwilliger, Advances, interactions, and future developments in the CNS, Phenix, and Rosetta structural biology software systems. *Annu. Rev. Biophys.* **42**, 265–287 (2013). doi:10.1146/annurev-biophys-083012-130253 Medline

67. P. Emsley, B. Lohkamp, W. G. Scott, K. Cowtan, Features and development of Coot. *Acta Crystallogr. D Biol. Crystallogr.* **66**, 486–501 (2010). doi:10.1107/S0907444910007493 Medline

68. A. J. McCoy, Solving structures of protein complexes by molecular replacement with Phaser. *Acta Crystallogr. D Biol. Crystallogr.* **63**, 32–41 (2007). doi:10.1107/S0907444906045975 Medline

69. P. V. Afonine, R. W. Grosse-Kunstleve, N. Echols, J. J. Headd, N. W. Moriarty, M. Mustyakimov, T. C. Terwilliger, A. Urzhumtsev, P. H. Zwart, P. D. Adams, Towards automated crystallographic structure refinement with phenix.refine. *Acta Crystallogr. D Biol. Crystallogr.* **68**, 352–367 (2012). doi:10.1107/S0907444912001308 Medline

70. V. B. Chen, W. B. Arendall III, J. J. Headd, D. A. Keedy, R. M. Immormino, G. J. Kapral, L. W. Murray, J. S. Richardson, D. C. Richardson, MolProbity: All-atom structure validation for macromolecular crystallography. *Acta Crystallogr. D Biol. Crystallogr.* **66**, 12–21 (2010). doi:10.1107/S0907444909042073 Medline

71. T. G. Battye, L. Kontogiannis, O. Johnson, H. R. Powell, A. G. Leslie, iMOSFLM: A new graphical interface for diffraction-image processing with MOSFLM. *Acta Crystallogr. D Biol. Crystallogr.* **67**, 271–281 (2011). doi:10.1107/S0907444910048675 Medline

72. J. Jumper, R. Evans, A. Pritzel, T. Green, M. Figurnov, O. Ronneberger, K. Tunyasuvunakool, R. Bates, A. Žídek, A. Potapenko, A. Bridgland, C. Meyer, S. A. A. Kohl, A. J. Ballard, A. Cowie, B. Romera-Paredes, S. Nikolov, R. Jain, J. Adler, T. Back, S. Petersen, D. Reiman, E. Clancy, M. Zielinski, M. Steinegger, M. Pacholska, T. Berghammer, S. Bodenstein, D. Silver, O. Vinyals, A. W. Senior, K. Kavukcuoglu, P. Kohli, D. Hassabis, Highly accurate protein structure prediction with AlphaFold. *Nature* **596**, 583–589 (2021). doi:10.1038/s41586-021-03819-2 Medline

73. T. I. Croll, ISOLDE: A physically realistic environment for model building into low-resolution electron-density maps. *Acta Crystallogr. D Struct. Biol.* **74**, 519–530 (2018). doi:10.1107/S2059798318002425 Medline

74. A. Punjani, J. L. Rubinstein, D. J. Fleet, M. A. Brubaker, cryoSPARC: Algorithms for rapid unsupervised cryo-EM structure determination. *Nat. Methods* **14**, 290–296 (2017). doi:10.1038/nmeth.4169 Medline

75. E. F. Pettersen, T. D. Goddard, C. C. Huang, E. C. Meng, G. S. Couch, T. I. Croll, J. H. Morris, T. E. Ferrin, UCSF ChimeraX: Structure visualization for researchers, educators, and developers. *Protein Sci.* **30**, 70–82 (2021). doi:10.1002/pro.3943 Medline

76. P. V. Afonine, B. K. Poon, R. J. Read, O. V. Sobolev, T. C. Terwilliger, A. Urzhumtsev, P. D. Adams, Real-space refinement in PHENIX for cryo-EM and crystallography. *Acta Crystallogr. D Struct. Biol.* **74**, 531–544 (2018). doi:10.1107/S2059798318006551 Medline

77. X. Zhang, R. Henriques, S. S. Lin, Q. W. Niu, N. H. Chua, Agrobacterium-mediated transformation of *Arabidopsis thaliana* using the floral dip method. *Nat. Protoc.* **1**, 641–646 (2006). doi:10.1038/nprot.2006.97 Medline

78. S. Asai, K. Ohta, H. Yoshioka, MAPK signaling regulates nitric oxide and NADPH oxidase-dependent oxidative bursts in *Nicotiana benthamiana*. *Plant Cell* **20**, 1390–1406 (2008). doi:10.1105/tpc.107.055855 Medline

79. T. Asai, G. Tena, J. Plotnikova, M. R. Willmann, W. L. Chiu, L. Gomez-Gomez, T. Boller, F. M. Ausubel, J. Sheen, MAP kinase signalling cascade in *Arabidopsis* innate immunity. *Nature* **415**, 977–983 (2002). doi:10.1038/415977a Medline

80. N. R. Baker, Chlorophyll fluorescence: A probe of photosynthesis in vivo. *Annu. Rev. Plant Biol.* **59**, 89–113 (2008). doi:10.1146/annurev.arplant.59.032607.092759 Medline

81. H. Ashkenazy, S. Abadi, E. Martz, O. Chay, I. Mayrose, T. Pupko, N. Ben-Tal, ConSurf 2016: An improved methodology to estimate and visualize evolutionary conservation in macromolecules. *Nucleic Acids Res.* **44**, W344–W350 (2016). doi:10.1093/nar/gkw408 Medline

82. J. A. Dongus, J. E. Parker, EDS1 signalling: At the nexus of intracellular and surface receptor immunity. *Curr. Opin. Plant Biol.* **62**, 102039 (2021). doi:10.1016/j.pbi.2021.102039 Medline

83. M. Zhang, Y. H. Chiang, T. Y. Toruño, D. Lee, M. Ma, X. Liang, N. K. Lal, M. Lemos, Y. J. Lu, S. Ma, J. Liu, B. Day, S. P. Dinesh-Kumar, K. Dehesh, D. Dou, J. M. Zhou, G. Coaker, The MAP4 kinase SIK1 ensures robust extracellular ROS burst and antibacterial immunity in plants. *Cell Host Microbe* **24**, 379–391.e5 (2018). doi:10.1016/j.chom.2018.08.007 Medline

84. H. Tian, Z. Wu, S. Chen, K. Ao, W. Huang, H. Yaghmaiean, T. Sun, F. Xu, Y. Zhang, S. Wang, X. Li, Y. Zhang, Activation of TIR signalling boosts pattern-triggered immunity. *Nature* **598**, 500–503 (2021). doi:10.1038/s41586-021-03987-1 Medline

85. C. J. Williams, J. J. Headd, N. W. Moriarty, M. G. Prisant, L. L. Videau, L. N. Deis, V. Verma, D. A. Keedy, B. J. Hintze, V. B. Chen, S. Jain, S. M. Lewis, W. B. Arendall III, J. Snoeyink, P. D. Adams, S. C. Lovell, J. S. Richardson, D. C. Richardson, MolProbity: More and better reference data for improved all-atom structure validation. *Protein Sci.* **27**, 293–315 (2018). doi:10.1002/pro.3330 Medline